

Integrated Design and Assessment of a Compact Axial Hydraulic Turbine

Dev Kumar, Thien Ho, Seyf Daab, Wilhem Abboura

▶ **To cite this version:**

Dev Kumar, Thien Ho, Seyf Daab, Wilhem Abboura. Integrated Design and Assessment of a Compact Axial Hydraulic Turbine. Independent research; original project at École Nationale Supérieure d'Arts et Métiers. 2026, pp.1-53. ⟨hal-05873043⟩

HAL Id: hal-05873043

https://hal.science/view/index/docid/5873043

Submitted on 19 Nov 2026

HAL is a multi-disciplinary open access archive for the deposit and dissemination of scientific research documents, whether they are published or not. The documents may come from teaching and research institutions in France or abroad, or from public or private research centers.

L'archive ouverte pluridisciplinaire **HAL**, est destinée au dépôt et à la diffusion de documents scientifiques de niveau recherche, publiés ou non, émanant des établissements d'enseignement et de recherche français ou étrangers, des laboratoires publics ou privés.



Copyright - All rights reserved

Integrated Design and Assessment of a Compact Axial Hydraulic Turbine

Hydraulic sizing, conversion chain and prototype testing
with reproducible numerical comparisons

Dev KUMAR, Thien HO, Seyf DAAB and Wilhem ABBOURA

École Nationale Supérieure d'Arts et Métiers

Paris, France

2024 engineering project
Experimental records and numerical study

Abstract

The 2024 compact axial-runner project is examined through hydraulic design, CFD, electromechanical conversion, prototype testing and industrial planning. A reconstructed 3.8 m design point and five radial velocity triangles agree with the archived MATLAB calculation. The selected CFD row gives a printed shaft power of 1.760 kW and water-side power of 5.160 kW under the same tabulated head and flow, implying 34.11%. The source efficiency column gives 74.74%. The recorded moment would give a tenfold higher shaft power at 1500 rpm. A conditional energy envelope shows that the 5 kW target exceeds the available water power at the original sizing flow. Independent switching simulations quantify separate carrier and inductance effects for a three-phase R–L model. The air-test coefficient of 0.239 implies 2.53 W under the reported tunnel conditions, which differ from the water design in tip-speed and Reynolds ratios. The 2 MW bulb-turbine fleet is evaluated separately with a deterministic production model and a cash-flow sensitivity. The original technical figures, equations and MATLAB routines accompany the study.

Keywords axial hydraulic turbine, Cordier diagram, blade geometry, CFD, power balance, permanent-magnet generator, PWM, tunnel similitude, production capacity.

Study record

Source [1] documents the 2024 engineering project. Source page numbers count the cover. Original plots and CAD views appear near their analyses and can be located through Appendix A. Original equations and tables are retained in Appendix B and MATLAB/XFoil listings in Appendix C. Three converter-study screenshots are cropped to the scientific windows. The source copy embedded in this manuscript applies the same crop.

Acknowledgements

Christophe Sarraf, Florent Ravelet, Pascal Caestecker and Jean-Frédéric Charpentier supervised the original project at École Nationale Supérieure d’Arts et Métiers.

Nomenclature

Symbol	Meaning
N, ω_m, p, ω_e	Mechanical rpm and angular speed, pole-pair count, electrical angular speed
N_{sq}, Ω_s, Λ	Engineering specific speed, dimensionless specific speed and radius
H, Q, $\dot{m}$, g	Net head, volume and mass flow rates, gravitational acceleration
R_e, R_i, r, A_a	Tip, hub and section radii, runner annular area
U, C_a, C_u	Blade peripheral speed, axial flow and whirl velocities
β_1, β_2, α_2	Blade inlet, outlet and discharge angle conventions
P_s, P_h, M, η	Shaft and water-side powers, torque and efficiency
B, H_m, B_r, B_1	Induction, magnetic field intensity, remanence and fundamental induction
g_m, e_a, D, L	Generator air gap, magnet thickness, gap diameter and active length
A_ℓ, J, i_d, i_q	Linear current loading, current density and synchronous-frame currents
R_s, V_{dc}, τ	Circuit resistance, DC-link voltage and R–L time constant
C_p, C_Q, λ, Re_D	Air-test power and torque coefficients, tip-speed ratio and Reynolds number

Contents

Abstract 1
Study record 1
Acknowledgements 1
Nomenclature 1
1. Introduction 3
2. Hydraulic preliminary design 3
2.1 Duty point and similarity variables 3
2.2 Cordier readout and choice of interpolation 4
2.3 Euler loading and velocity angles 6
2.4 Mean line, thickness and cylindrical projection 7
3. CAD and structural screening 9
3.1 From point clouds to the fluid domain 9
3.2 What the finite-element image establishes 10
4. CFD reconstruction and shaft power 11
4.1 Model and numerical evidence 11
4.2 Conservation equations and sheet-level checks 12
4.3 Power, torque and efficiency at the candidate point 14
4.4 The 5 kW requirement 14
5. Generator and converter modelling 15
5.1 Mechanical and electrical duty 15
5.2 Field, conductor EMF and mean torque 16
5.3 Magnet thickness and fundamental induction 17
5.4 Active length and thermal scale 18
5.5 Variable-speed control structure 19
5.6 PWM waveform and R–L check 19
5.7 Independently switched three-phase test 21
6. Prototype and wind-tunnel experiment 24
6.1 Manufacture and test configuration 24
6.2 Reconstructed aerodynamic point 26
6.3 Transfer limits 27
7. Industrial scenario and sensitivity 27
7.1 Product and regional scope 27
7.2 Fleet energy and production schedule 29
7.3 Takt, lead time and event model 29
7.4 Sourcing, cost reconciliation and finance 30
8. Conclusions 31
References 32
Appendix A. Original figure concordance 33
Appendix B. Original equations and tables 35
Appendix C. Original MATLAB and XFoil listings 42
Appendix D. Reproducibility 52
D.1 Running the Python study 52
D.2 Numerical checks 52

1. Introduction

The development study in [1] followed a low-head axial runner from preliminary sizing to a manufactured prototype. It combined MATLAB and XFoil section design, CATIA solid modelling and stress calculations, a STAR-CCM+ moving-reference-frame study, a surface-magnet generator and converter model, and a wind-tunnel experiment. A separate industrial scenario examined a fleet of MW-class bulb turbines. The engineering question is how evidence from these stages constrains the next design decision.

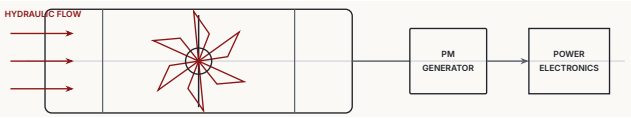

Figure 1.1 – Development chain shown on the original report cover. The rotor drives a permanent-magnet machine with a separate converter stage.

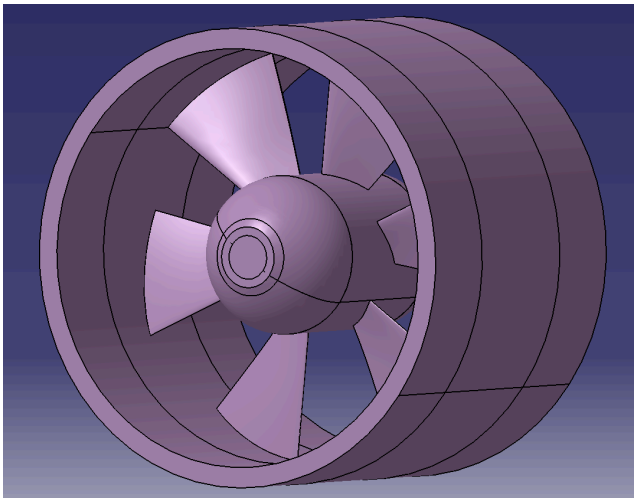

Figure 1.2 – Archived overview of the ducted axial-runner assembly. The detailed CAD sequence is shown in Section 3.

This manuscript tests the numerical consistency of the data passed between those stages. The printed CFD sweep is transcribed and checked against the shaft and hydraulic power equations. The MATLAB geometry is reconstructed independently, including the radial discretisation and blade thickness. A switching simulation varies carrier frequency and inductance separately. Aerodynamic measurements are interpreted in their own reference area and speed scale. The production and cash-flow assumptions are evaluated as a separate industrial scenario. None of these calculations uses unavailable CFD, Simulink or tunnel recording files.

The 57-page report [1] is the primary record. Its technical figures and four MATLAB listings appear in this manuscript. The original displayed relations and supporting tables are reproduced in the appendices. The accompanying Python calculations use stated inputs and are reproducible from the code embedded in the PDF. Terms used across domains are distinguished explicitly. In particular, ω_m is mechanical angular speed, Ω_s denotes dimensionless hydraulic specific speed, and g_m is the generator air gap.

2. Hydraulic preliminary design

2.1 Duty point and similarity variables

The specification in [1] sets a nominal speed of 1500 rpm, engineering specific speed N_{sq}=200, upper head of 4 m and outer radius R_e=0.103 m. The duty-point geometry uses a hub-to-tip ratio of 0.38. The CFD work also starts with a 5 kW shaft target and a 92% hydraulic efficiency assumption. Those two target values do not establish the available water energy.

For a specified flow Q, net total head H and radius R, the dimensionless variables are

$$\begin{aligned} \omega_m &= \frac{2\pi N}{60}, \\ N_{sq} &= \frac{N\sqrt{Q}}{H^{3/4}} \\ \Omega_s &= \frac{\omega_m \sqrt{Q}}{(gH)^{3/4}} \\ &= \frac{2\pi N_{sq}}{60 g^{3/4}} \\ \Lambda &= \frac{R(gH)^{1/4}}{\sqrt{Q}}. \end{aligned} \tag{1}$$

The engineering speed index depends on using rpm, metres and cubic metres per second as stated. Taking the dimensionless flow and head coefficients on the radius scale as $\Phi = Q/(\omega_m R^3)$ and $\Psi = gH/(\omega_m^2 R^2)$ gives $\Omega_s = \Phi^{1/2}/\Psi^{3/4}$ and $\Lambda = \Psi^{1/4}/\Phi^{1/2}$. These relations are the similarity basis of the Cordier selection [2]. Multiplication eliminates the unknown discharge and yields a closed-form head estimate:

$$\begin{aligned} \Omega_s \Lambda &= \frac{\omega_m R}{\sqrt{gH}}, \\ H &= \frac{1}{g}\left(\frac{\omega_m R}{\Omega_s \Lambda}\right)^2 \\ Q &= \left(\frac{N_{sq}}{N}\right)^2 H^{3/2}. \end{aligned} \tag{2}$$

The result is one compatible design point when speed, radius and both similarity coordinates are fixed. The equation for Q(H) at fixed N_{sq} alone should therefore not be treated as an off-design runner performance curve. It follows that near a given Cordier selection, a fractional change in Λ contributes twice that change with opposite sign to H, and three times with opposite sign to Q, holding the other inputs fixed.

2.2 Cordier readout and choice of interpolation

Figure 2.1 records the digitised Kaplan region. Figure 2.2 has logarithmic axes and identifies end points near (0.2804,9.224) and (1.31,1.987). The text of [1] uses the slope from those two points with an intercept of 8.705. At Ω_s=3.77839, this gives Λ=0.70090, agreeing with the archived MATLAB input of 0.701. The intercept of the straight line actually passing through both end points is 11.19492. A straight secant in linear coordinates and a secant in logarithmic coordinates therefore produce different answers. The code selection is kept explicitly instead of replacing it with a new digitisation.

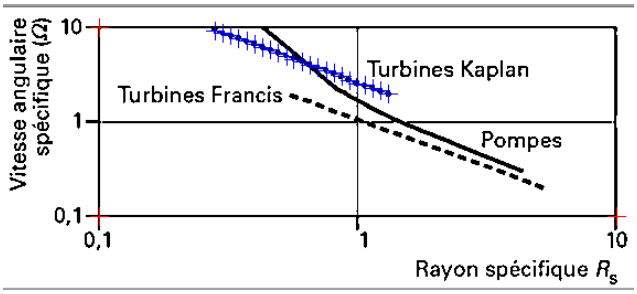

Figure 2.1 – Original digitisation of the Kaplan region, as archived in [1]. The reference curve is used for preliminary similarity sizing. Source Fig. 2.1, p. 9 of [1].

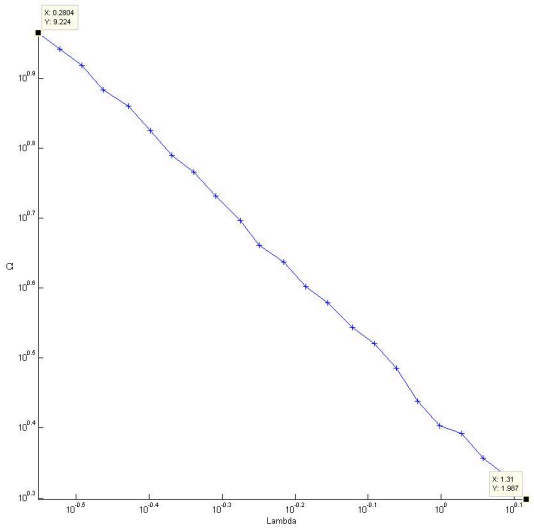

Figure 2.2 – Archived MATLAB display of the digitised point sequence. The two end markers provide the numerical inputs to Table 2.1. Source Fig. 2.2, p. 10 of [1].

Table 2.1 – Hydraulic sizing from the archived specific radius and two end-point interpolation choices. All use N = 1500 rpm and the same radius.

Radius selection	Λ	H (m)	Q (m³/s)
MATLAB input	0.70100	3.804	0.13188
Printed line and intercept	0.70090	3.805	0.13193
Linear secant	1.05514	1.679	0.03867
Log–log secant	0.68707	3.959	0.14006

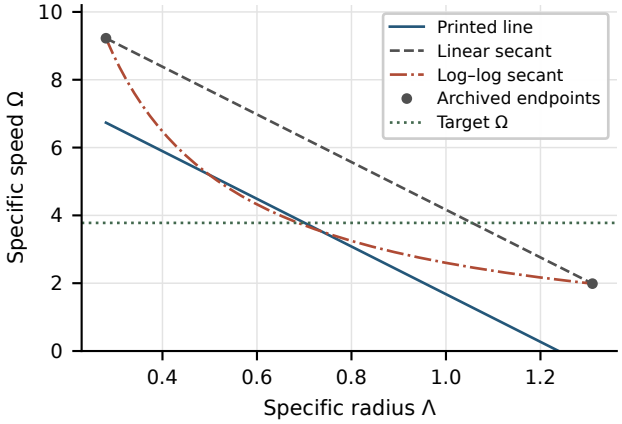

Figure 2.3 – Python. The archived straight-line equation, the end-point secant in linear coordinates and the end-point secant in logarithmic coordinates. Only the two annotated points are used in the two sensitivity cases.

The log–log secant gives a head of 3.96 m and a flow of 0.1401 m³/s, compared with 3.804 m and 0.1319 m³/s at the coded radius index. The straight secant in linear coordinates is a much larger departure, with a head near 1.68 m. These comparisons show the dependence on the interpolation rule, including the importance of the original plot coordinates. Neither comparison constitutes a performance measurement, and the two end points cannot identify the curvature of the digitised locus.

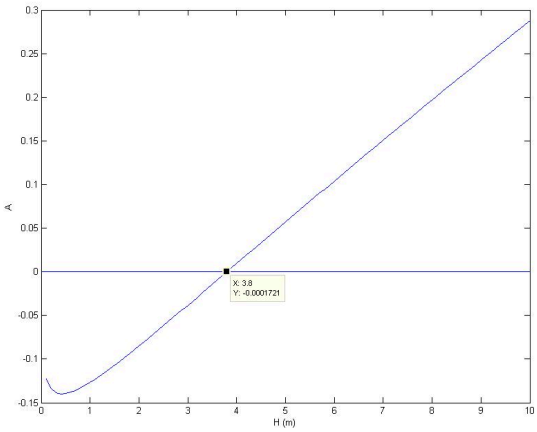

Figure 2.4 – Original intersection used to choose a head near 3.8 m. The abscissa marks the zero of the difference between two expressions for the square root of the discharge. Source Fig. 2.3, p. 11 of [1].

The archived script rounds the head to 3.8 m before calculating the remaining dimensions. It gives Q=0.131690 m³/s. The exact hub radius is 0.03914 m. The MATLAB implementation floors this to 0.039 m and floors the five radial stations to the millimetre. The axial speed across the annular flow area is

$$R_i = 0.38 R_e, \qquad A_a = \pi (R_e^2 - R_i^2)$$
$$C_a = \frac{Q}{A_a}. \tag{3}$$

Using the rounded flow 0.132 m³/s with the unrounded radius gives 4.629 m/s, as printed in the text. Using the script flow with the floored hub gives 4.6125 m/s, as in the MATLAB screenshot. Using the unrounded radius and script flow gives 4.6180 m/s. All three values are tied to specific conventions and need not be interchanged in a velocity-triangle calculation.

2.3 Euler loading and velocity angles

The velocity triangles assume zero incoming swirl, constant axial speed and no change in radius across a blade section. For positive extraction and the sign conventions of the archived code, the Euler relation [2] gives a negative outlet whirl.

$$\begin{aligned} U(r) &= \omega_m r, \qquad C_{u,1} = 0 \\ w &= U(C_{u,1} - C_{u,2}) \\ C_{u,2,\mathrm{th}} &= -gH/U, \\ C_{u,2} &= \eta_h C_{u,2,\mathrm{th}}. \end{aligned} \tag{4}$$

The symbol η_h in (4) is the 0.92 sizing coefficient used in the MATLAB script. Under these assumptions, $-U\,C_{u,2}$ is constant across the radius. This prescribes a spanwise work distribution. It does not imply equal local incidence, pressure, losses or degree of reaction.

$$\begin{aligned} \beta_1 &= \arctan(U/C_a) \\ \beta_2 &= \arctan[(U - C_{u,2})/C_a] \\ \alpha_2 &= \arctan(C_a/C_{u,2}). \end{aligned} \tag{5}$$

The last equation gives the one-argument arctangent branch in the MATLAB listing. If a directed azimuthal angle is required, the quadrant must be resolved using both velocity components. The radial screenshot in Figure 2.5 reports positive whirl magnitudes and a column labelled corrected whirl that is approximately the theoretical column divided by 0.92. This differs from the signed multiplication in the listing. For example, the root row displays 5.904 and 6.418 m/s. Their ratio is about 0.920. The screen also uses ten samples, whereas the archived angle listing takes five. Its columns are retained without substituting them for the specified MATLAB run.

Rayon (r) [m]	U(r) [m/s]	Cu_th(r) [m/s]	Cu(r) [m/s]
0,039	6,148	5,904	6,418
0,046	7,262	4,998	5,433
0,053	8,377	4,333	4,710
0,060	9,491	3,824	4,157
0,068	10,606	3,422	3,720
0,075	11,720	3,097	3,366
0,082	12,835	2,828	3,074
0,089	13,949	2,602	2,828
0,096	15,064	2,410	2,619
0,103	16,178	2,244	2,439

Figure 2.5 – Archived radial velocity table. Its whirl columns use the positive-magnitude display and the original labels. Source Fig. 2.4, p. 11 of [1].

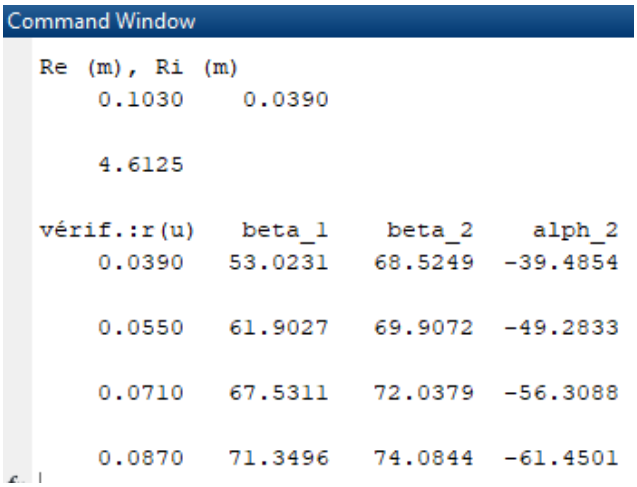

Figure 2.6 – Archived MATLAB Command Window check. The displayed axial velocity and the first four rows can be recovered from the 3.8 m input, floored radii and signed whirl in the code. Source Fig. 2.5, p. 12 of [1].

Table 2.2 – Five-station reconstruction of the coded velocity triangles. Speed is in m/s and angles are in degrees.

r (mm)	U	$C_{u,2}$	β_1	β_2	α_2
39	6.126	−5.598	53.023	68.525	−39.485
55	8.639	−3.970	61.903	69.907	−49.283
71	11.153	−3.075	67.531	72.038	−56.309
87	13.666	−2.510	71.350	74.084	−61.450
103	16.179	−2.120	74.088	75.853	−65.318

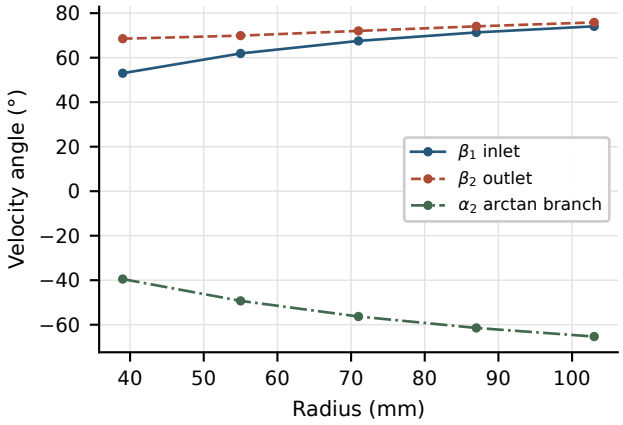

Figure 2.7 – Python. Five-station angles reconstructed from the archived MATLAB expressions. The negative discharge angle is the original arctangent branch.

At the first station, 39 mm, the reconstructed angles are 53.0231°, 68.5249° and −39.4854°. The screenshot contains these values. The inlet and outlet angles remain inside the declared 30–80° design window across the five stations. Because the outlet whirl magnitude decreases approximately as 1/r, the difference between the two blade angles reduces towards the tip. The result reproduces the design convention and its calculation. The actual three-dimensional inflow and exit swirl require flow-field measurements or saved CFD surface reports.

2.4 Mean line, thickness and cylindrical projection

In the MATLAB function *ligneK*, the local tangent varies linearly with the dimensionless axial abscissa x. If $m_1=\tan\beta_1$ and $m_2=\tan\beta_2$, then

$$\begin{aligned} y_c'(x) &= m_1 + (m_2 - m_1)x \\ y_c(x) &= m_1 x + \tfrac{1}{2}(m_2 - m_1)x^2 \\ \beta(x) &= \arctan y_c'(x), \quad 0 \le x \le 1. \end{aligned} \tag{6}$$

This construction exactly reaches the chosen slopes at the two ends. The prose equation of [1] shows an additional “2” next to the normalised coordinate. The archived function and the reconstructed geometry use (6). The printed expression is preserved in Appendix B.

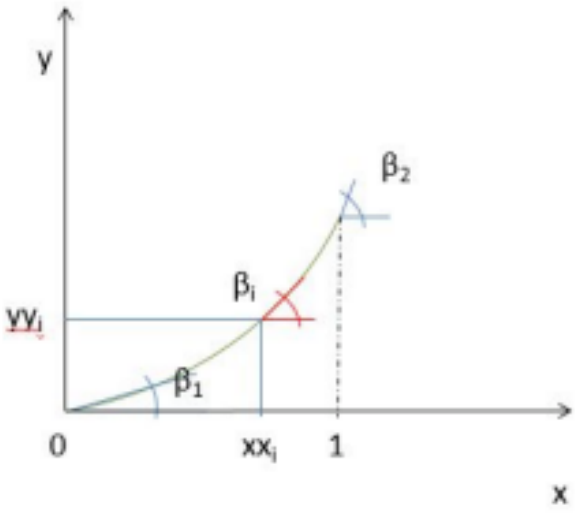

Figure 2.8 – Original blade mean-line and tangent construction. Source Fig. 2.6, p. 12 of [1].

The original workflow increases the thickness of a NACA-type section and fits a five-term law to the upper-surface points exported from XFoil. For input relative thickness t_r, with coefficients $a_0,\ldots,a_4$, it uses

$$\begin{aligned} f(x) &= a_0\sqrt{x} + a_1 x + a_2 x^2 + a_3 x^3 + a_4 x^4 \\ y_t(x) &= \frac{t_r}{0.2} f(x) \\ E(a) &= \sum_j [y_j - y_t(x_j; a)]^2. \end{aligned} \tag{7}$$

The complete routines and filenames appear in Appendix C. The source uses *fminsearch* on the squared residual, and the fit itself is linear in the five coefficients. A least-squares solve would be an independent way to recover the coefficients if the XFoil point file were available. With only the recorded vector, the Python calculation reconstructs the sections and reports the geometric implications. It does not refit the original data or infer the fit residual.

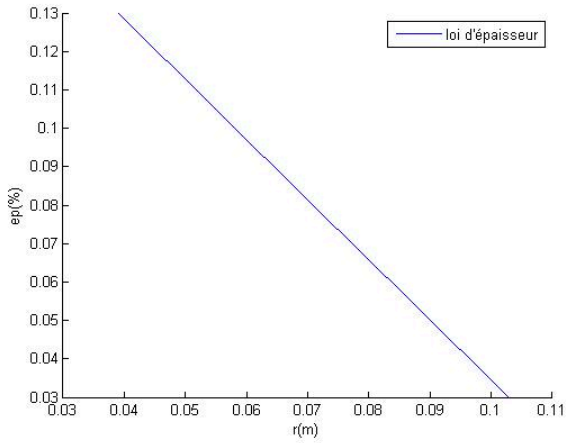

Figure 2.9 – Original hub-to-tip thickness schedule. The code decreases the section input from 13% to 3%. Source Fig. 2.7, p. 13 of [1].

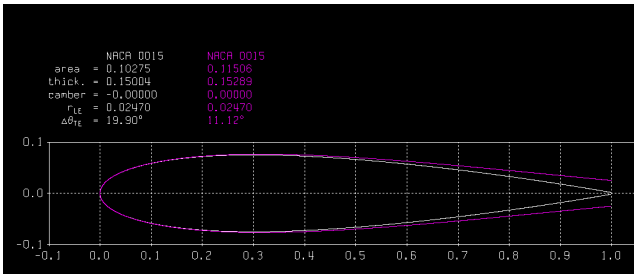

Figure 2.10 – Archived comparison between the initial profile and the thicker modification used to prepare the fit. Source Fig. 2.8, p. 13 of [1].

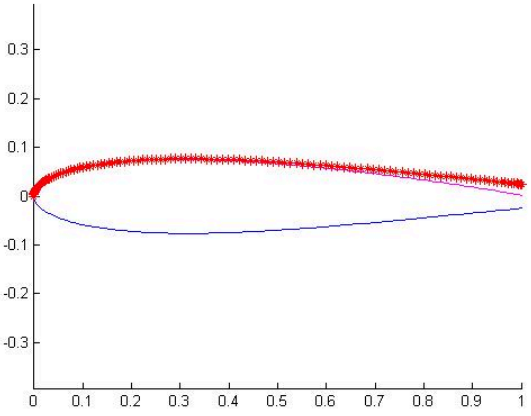

Figure 2.11 – Original fit display and overlaid point sets. The source point file is needed to quantify any residual. Source Fig. 2.9, p. 13 of [1].

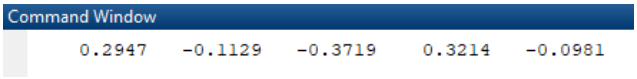

Figure 2.12 – Archived fitted polynomial coefficients. They are used verbatim in the independent reconstruction. Source Fig. 2.10, p. 14 of [1].

Let $c_0=\sqrt{(1+y_c(1)^2)}$ and $n=(-\sin\beta,\cos\beta)$. The MATLAB function offsets the chord-normalised mean line on each side along this local normal. It uses six blades and a solidity $\sigma_b=0.60$, so its physical chord scale is $c=\sigma_b\, 2\pi\, r/6$. The blade envelope in the cylindrical coordinate system follows by converting the scaled tangential coordinate s_t to azimuth. The dimensional export multiplies the resulting metre coordinates by 1000 for CATIA.

$$(x_\pm, y_\pm) = (x, y_c)/c_0 \pm y_t n$$
$$c = \sigma_b \frac{2\pi r}{Z_b}, \qquad \theta = s_t / r \tag{8}$$
$$(X, Y, Z) = (s_a, r\cos\theta, r\sin\theta).$$

The recorded vector is $(0.2947,-0.1129,-0.3719,0.3214,-0.0981)$. Its sum is 0.0332, so the trailing-edge normal thickness is finite. The values implied by the root and tip sections are about 1.06 and 0.64 mm, before lofting or print slicing. These are distances between the two envelope points of the normal-offset law. They are not tolerance or stress limits.

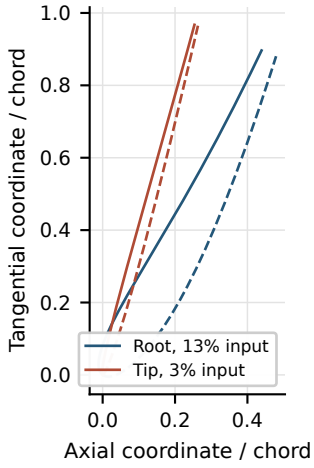

Figure 2.13 – Python. Root and tip chord-normalised sections calculated from the archived camber and thickness functions. Their stagger differs because the velocity angles differ with radius.

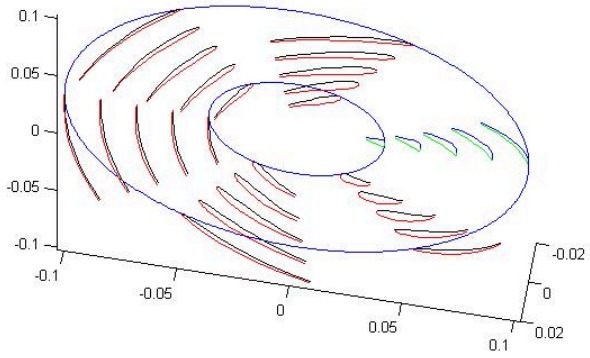

Figure 2.14 – Original blade-row geometry after section scaling, cylindrical projection and circumferential replication. Source Fig. 2.11, p. 14 of [1].

3. CAD and structural screening

3.1 From point clouds to the fluid domain

The MATLAB export writes consecutive upper- and lower-surface point sets between curve and loft markers. The workflow imports them into CATIA V5 Generative Shape Design, creates blade surfaces, then constructs the complete runner in Part Design by a sixfold circular pattern. The principal drawing shows a diameter of 206 mm, a hub radius marked 39 mm and axial segments of 45, 75 and 45 mm. The drawing is consistent with the rounded CAD dimensions used for runner assembly. The CAD panels retain the main point-transfer and assembly stages.

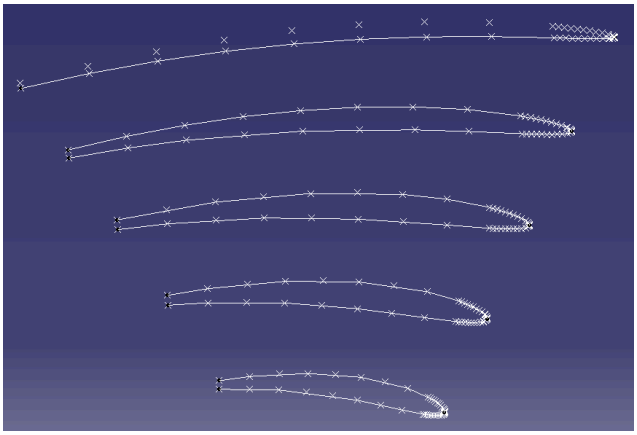

Figure 3.1a – Original MATLAB surface point curves before export. Source Fig. 3.1a, p. 15 of [1].

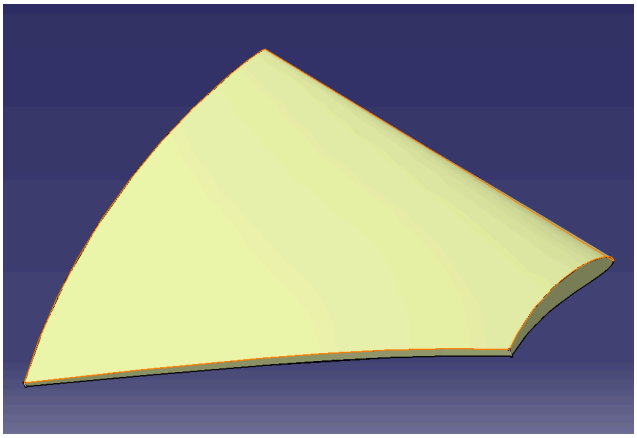

Figure 3.1b – Original blade surface rebuilt in CATIA V5 from the section data. Source Fig. 3.1b, p. 15 of [1].

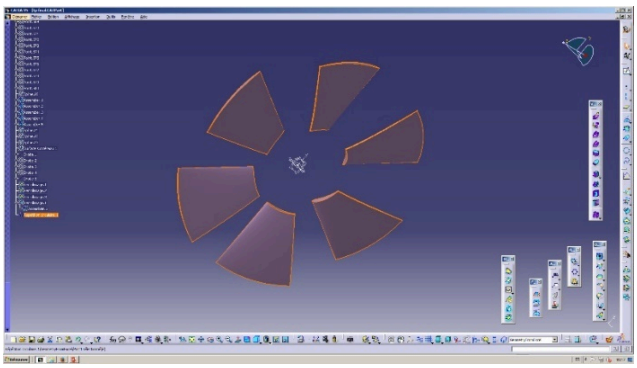

Figure 3.2a – Circumferential duplication of the blade in the rotor assembly. Source Fig. 3.3a, p. 16 of [1].

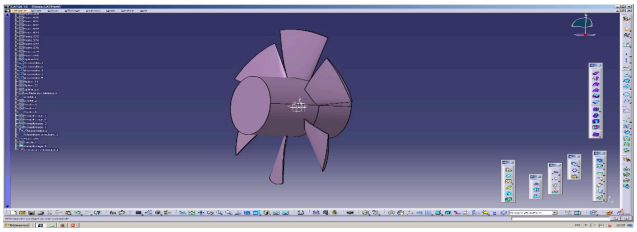

Figure 3.2b – Original integration of runner blades and hub. Source Fig. 3.3b, p. 16 of [1].

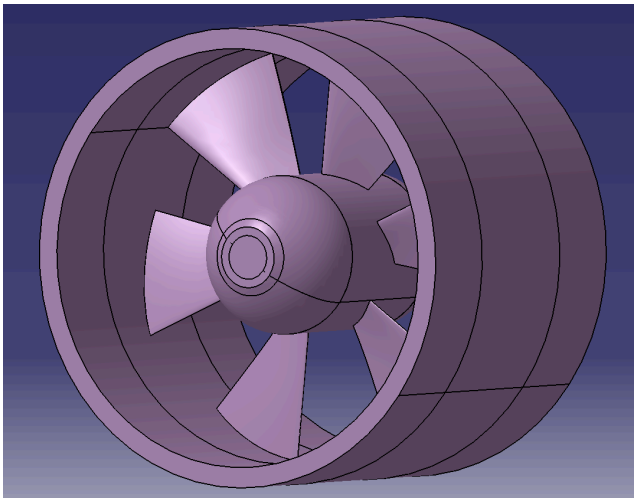

Figure 3.3 – Full ducted assembly in the archived CAD model. Source Fig. 3.4, p. 16 of [1].

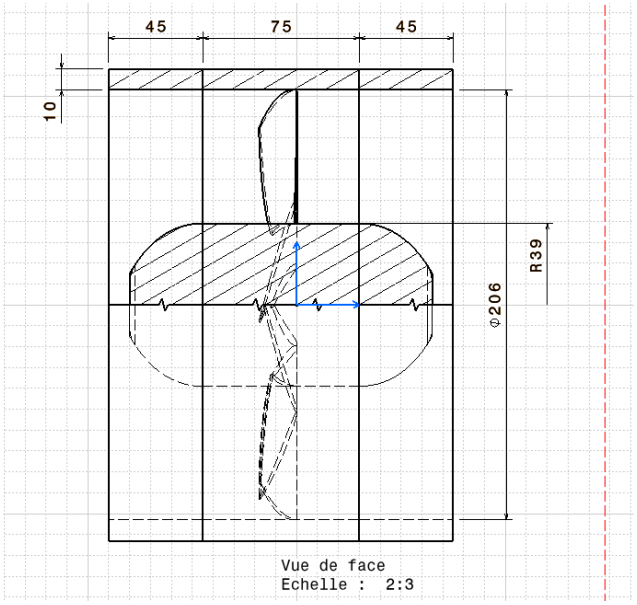

Figure 3.4 – Archived dimensioned drawing. The bore diameter and axial segmentation identify the principal model dimensions. Source Fig. 3.5, p. 17 of [1].

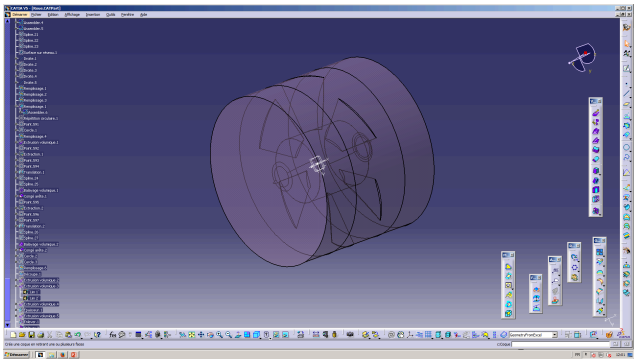

Figure 3.5 – Fluid volumes cut from the assembled solids for the CFD model. Source Fig. 3.6, p. 17 of [1].

The duct is separated into upstream, rotating and downstream regions, which permits reference-frame changes and boundary placement away from the runner. Axial lengths in the solid drawing should be distinguished from the extended computational inlet and outlet sections. Blade-tip clearance, surface finish and transition fillets are relevant to both flow and stress. The archived images do not provide tolerances or a watertight CAD export for independent model replication.

3.2 What the finite-element image establishes

The archived calculation fixes the root and applies distributed tractions to the blade surfaces. The equivalent-stress field concentrates near the support. The colour bar in Figure 3.6 is labelled N/m² and reaches approximately 3.03×10^{11} Pa. The narrative in [1] describes stresses below the elastic limit, but supplies neither the allowable stress nor a model result that reconciles this scale. The image can locate the displayed concentration. It cannot establish an elastic safety margin from the available data.

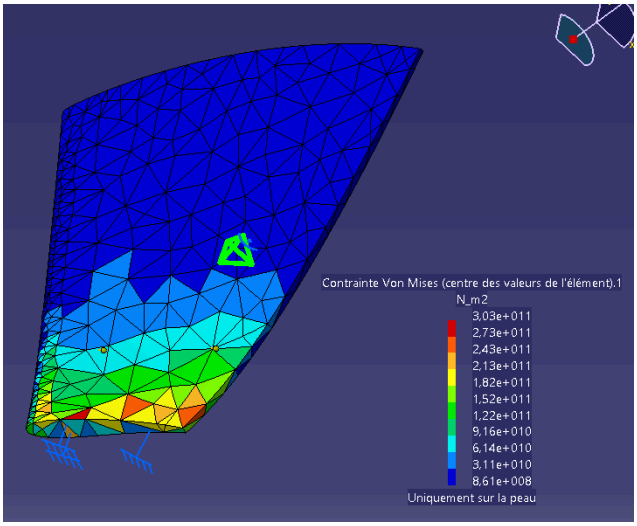

Figure 3.6 – Original equivalent-stress field. The archived legend reaches about 303 GPa as labelled. Load units, material values and mesh behaviour at the fixed root require confirmation. Source Fig. 3.2, p. 16 of [1].

For a follow-on comparison between meshes, one can integrate surface pressure and traction to obtain root force and moment. Taking r_0 at a specified root section and t the applied traction on the blade surface A_b,

$$F = \int_{A_b} t\, dA, \qquad M_0 = \int_{A_b} (r - r_0) \times t\, dA. \tag{9}$$

A nominal bending estimate M_0 c/I, where I is the section second moment and c the outer-fibre distance, is then a useful order-of-magnitude comparison. The peak element value at a fully fixed edge can be sensitive to artificial constraint geometry and local refinement. A comparison would require a material model, physical root geometry, pressure reference, converged stress away from the fixity and a documented load case. The PLA tunnel demonstration and the blade FEA use different load and material contexts.

4. CFD reconstruction and shaft power

4.1 Model and numerical evidence

Source [1] describes a segregated formulation, steady moving-reference-frame treatment and a pressure reference of 101,300 Pa. The initial mesh is reported as 61,518 cells, 279,251 faces and 187,548 vertices. The extended domain includes separate rotating and stationary regions. A steady calculation is sufficient to explore a tentative mean operating point under its model assumptions. Interaction at interfaces, wake unsteadiness, clearance leakage and resolved wall stress depend on the modelling and mesh details.

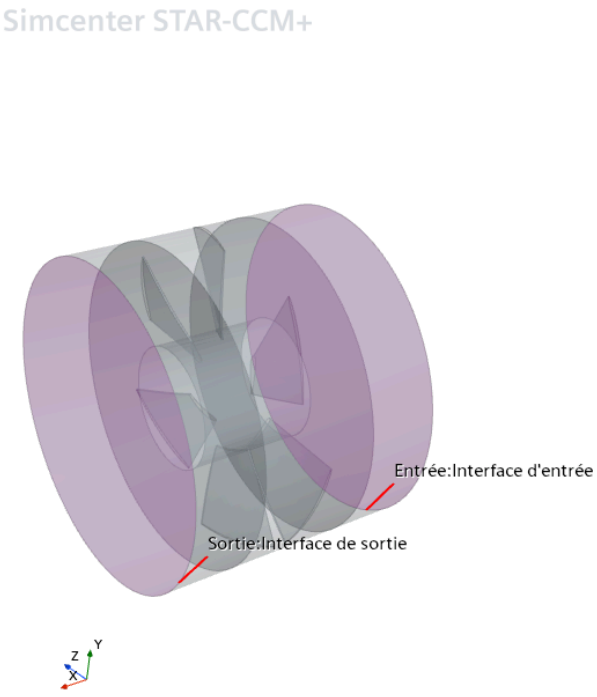

Figure 4.1a – Original inlet, rotating interfaces and outlet defined for the CFD domain. Source Fig. 4.1a, p. 18 of [1].

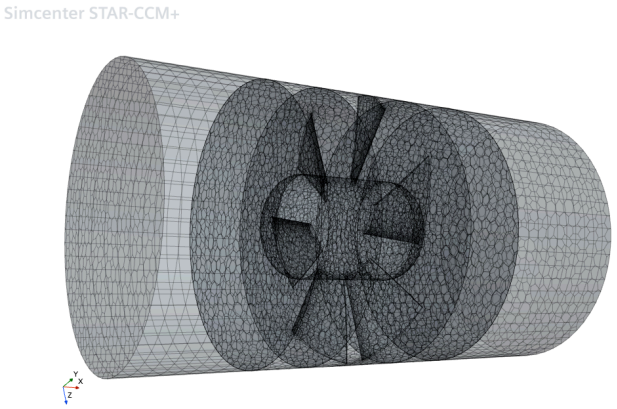

Figure 4.1b – Archived surface and volume mesh view. Source Fig. 4.1b, p. 18 of [1].

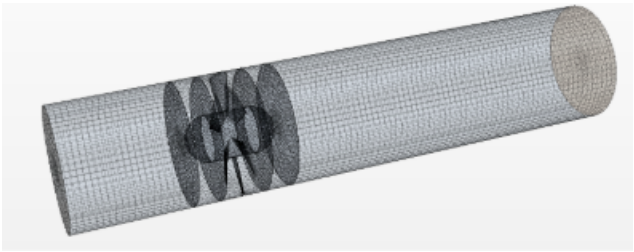

Figure 4.2 – Mesh detail in the rotating runner region. Source Fig. 4.2, p. 19 of [1].

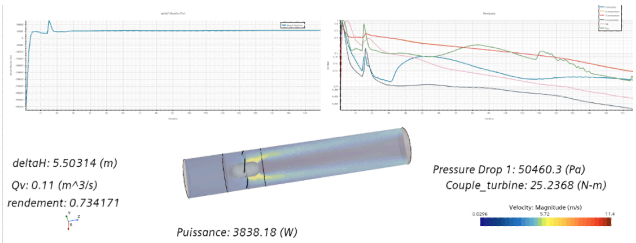

Figure 4.3a – Archived monitor, residual plot and annotated operating case. This panel labels a head of 5.503 m, outside the design specification of at most 4 m. Source Fig. 4.3a, p. 19 of [1].



Figure 4.3b – Section through the discretised fluid domain, placed alongside the convergence panel in [1]. Source Fig. 4.3b, p. 19 of [1].

Source [1] states a budget of 1000 iterations and an expected residual below 10^{-3}. The plotted monitor shows a settled interval for one case, and the residual traces remain separate tests of the solved equations. Neither gives a spatial-discretisation error. A mesh study should track the same mass flow, mass-averaged head and integrated shaft torque across three systematic resolutions. A refinement ratio based on average cell size can be used with Richardson extrapolation and a grid convergence index if the observed series supports it [3]. The archive supplies one quantified mesh, so no such error band is calculated here.

The combined convergence panel is its own numeric case. It displays $Q \approx 0.11$ m³/s, $H = 5.50314$ m, $\Delta p = 50{,}460.3$ Pa, $M = 25.2368$ N·m and $P = 3838.18$ W alongside a reported efficiency of 0.734171. Its quotient $P/M = 152.09$ rad/s differs from 1500 rpm converted to mechanical speed. The operating point lies above the specified 4 m envelope and is kept separate from the later eight-row sweep.

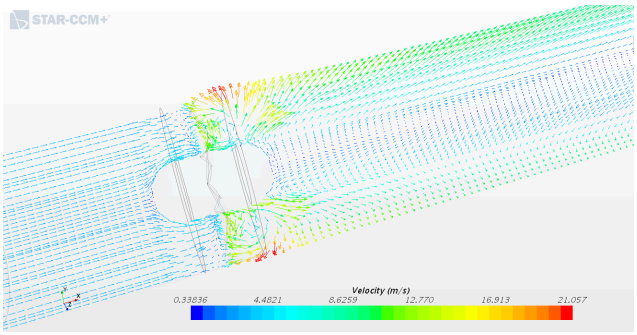

Figure 4.4 – Original velocity-vector field through the runner and wake. The scale refers to velocity magnitude. An absolute pressure field is required for cavitation assessment. Source Fig. 4.4, p. 19 of [1].

An appropriate cavitation check would compare the minimum local absolute pressure to the vapour pressure at the recorded water temperature. Gauge, static and total-pressure fields must be distinguished and the operating head established. The source shows velocities and states a reference pressure but supplies no recoverable minimum absolute blade pressure or cavitation test. Thus the field identifies locations of acceleration and the wake while leaving cavitation margin open.

4.2 Conservation equations and sheet-level checks

For a shaft torque M and mechanical speed ω_m, $P_s = M\omega_m$. If H_n is the net total-head drop across the same control volume and the fluid is incompressible, $P_h = \rho_w g Q H_n$. In a uniform

one-dimensional comparison the total head includes the static-pressure, kinetic-energy and elevation terms.

$$P_s = M\omega_m, \qquad P_h = \rho_w g Q H_n$$
$$\eta_s = P_s / P_h, \qquad \dot{m} = \rho_w Q$$
$$H_n = \Delta\left(\frac{p}{\rho_w g} + \frac{V^2}{2g} + z\right). \tag{10}$$

In nonuniform CFD fields the appropriate velocity and pressure terms are taken on consistent surfaces, using the flux definition of energy. When only a static pressure drop is available, QΔ p is a comparison quantity. It equals head power only under conditions in which the other terms cancel or are already included in the pressure definition. Here both versions are evaluated using the archived columns, without assuming which estimator the original efficiency used.

N (RPM)	Qm (kg/s)	Rendement (%)	DeltaP (Pa)	DeltaP (bar)	DeltaH (m)	Moment (N.m)	Omega	Rho	Pm (W)	Qv (m³/s)
1500	111,1	67,67	12019	0,12019	1,2221	82,82	158,57	1010	1300,274	0,1111
1500	128,27	68,68	23836	0,23836	2,3836	99,586	158,57	1010	1563,48	0,12827
1500	131,3	71,71	26664	0,26664	2,6664	102,01	158,57	1010	1601,557	0,1313
1500	141,4	74,74	36057	0,36057	3,6057	112,11	158,57	1010	1760,127	0,14443
1500	146,45	72,72	41511	0,41511	4,1511	117,16	158,57	1010	1839,412	0,14645
1500	151,5	69,69	47470	0,4747	4,747	122,21	158,57	1010	1918,697	0,1515
1500	156,55	68,68	52520	0,5252	5,252	127,26	158,57	1010	1997,982	0,15655
1500	161,6	65,65	58479	0,58479	5,8479	132,31	158,57	1010	2077,267	0,1616

Figure 4.5 – Original eight-row spreadsheet from the STAR-CCM+ operating sweep. The reported peak-efficiency row is the fourth row, and the largest printed power is in the last row. Readable transcriptions appear in Tables 4.1 and 4.2. Source Fig. 4.5, p. 20 of [1].

The fourth row is labelled 1500 rpm, 0.14443 m³/s, 3.6057 m and 1760.127 W. It contains the largest printed efficiency, 74.74%. It also has the largest printed shaft power among the four rows below 4 m as tabulated. The eighth row gives a higher printed power, 2077.267 W, at a head of 5.8479 m. Thus the fourth row is a candidate under the stated head ceiling and the source's own ordering. The efficiency column must still be reconciled before inferring an actual optimum.

Table 4.1 – Literal CFD-sweep transcription of the principal printed fields. Density is 1010 kg/m³ and printed angular speed is 158.57 rad/s throughout.

Row	ṁ (kg/s)	Q (m³/s)	Δp (Pa)	H (m)	M (N·m)	P (W)	η (%)
1	111.10	0.11110	12019	1.2221	82.820	1300.274	67.67
2	128.27	0.12827	23836	2.3836	99.586	1563.480	68.68
3	131.30	0.13130	26664	2.6664	102.010	1601.557	71.71
4	141.40	0.14443	36057	3.6057	112.110	1760.127	74.74
5	146.45	0.14645	41511	4.1511	117.160	1839.412	72.72
6	151.50	0.15150	47470	4.7470	122.210	1918.697	69.69
7	156.55	0.15655	52520	5.2520	127.260	1997.982	68.68
8	161.60	0.16160	58479	5.8479	132.310	2077.267	65.65

Table 4.2 – Checks derived from the CFD row fields. Head-based and pressure-based efficiencies use the printed power and volume flow. The torque is inferred from 1500 rpm, not the moment column.

Row	ṁ/ρ (m³/s)	P_h (kW)	ΔpQ (kW)	M from P (N·m)	η_H (%)	$\eta_{\Delta p}$ (%)
1	0.11000	1.345	1.335	8.278	96.65	97.38
2	0.12700	3.029	3.057	9.953	51.61	51.14
3	0.13000	3.469	3.501	10.196	46.17	45.75
4	0.14000	5.160	5.208	11.205	34.11	33.80
5	0.14500	6.023	6.079	11.710	30.54	30.26
6	0.15000	7.126	7.192	12.215	26.93	26.68
7	0.15500	8.146	8.222	12.720	24.53	24.30
8	0.16000	9.363	9.450	13.224	22.19	21.98

At that row, $\dot{m}$=141.4 kg/s and ρ_w=1010 kg/m³ imply Q=0.14000 m³/s. The printed volumetric flow is 3.16% higher than the mass-derived value. The source pressure difference of 36,057 Pa gives 3.639 m of static head for the printed density and g=9.81 m/s², versus the printed head of 3.6057 m. Most displayed head entries are close to division of pressure drop by 10,000 Pa/m. The records do not establish whether a velocity-head correction was included.

4.3 Power, torque and efficiency at the candidate point

Multiplication of the printed moment, 112.11 N·m, by the speed derived from 1500 rpm gives 17.61 kW. The printed power is 1.760 kW. In all eight rows, the value of P_s/M is approximately 15.70 rad/s. The speed printed elsewhere in the same rows is 158.57 rad/s, while the conversion of 1500 rpm gives 157.08 rad/s. The observed factor of ten is consequently a unit or scale issue in at least one reported field. At 1500 rpm the 1.760 kW value implies a torque of 11.205 N·m. As printed in newton-metres, the 112.11 N·m value would exceed the available hydraulic power for either reconstructed head definition in the same row.

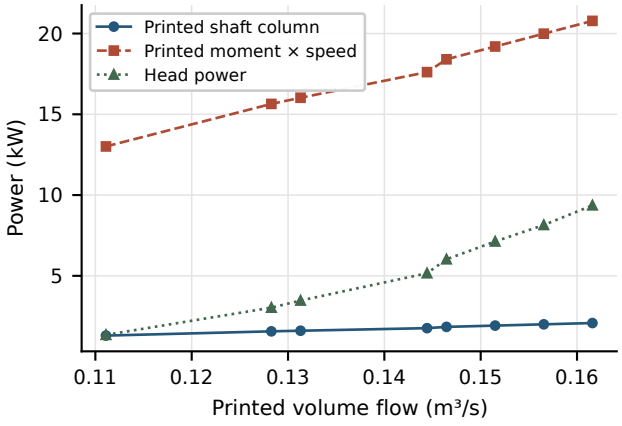

Figure 4.6 – Python. Printed shaft power, torque-times-speed using the moment labels as written, and water-side power using the reported head. The three curves reuse the transcribed rows and contain no new CFD outputs.

Using the literal fourth-row density, volume flow and head gives P_h=5.160 kW and P_s/P_h=34.11%. Using the pressure-flow product instead gives 5.208 kW and 33.80%. Using the rounded prose values, fresh water of 1000 kg/m³ and 3.60 m at 0.144 m³/s, gives 34.61%. These calculated values are conditional efficiencies under the respective definitions. The archived 74.74% is incompatible with the same reported shaft power and either of the two direct water-side powers. Resolving it requires the original pressure averages, torque units and monitor definitions. No efficiency maximum or mesh independence is inferred from this spreadsheet.

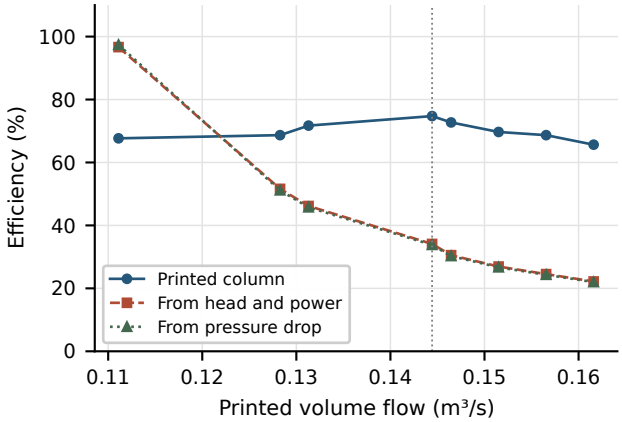

Figure 4.7 – Python. The archived efficiency column and two recalculations on the same reported flow axis. The vertical marker identifies row four. Connecting lines guide the eye between the eight stored cases.

4.4 The 5 kW requirement

Before flow losses, the 3.8 m sizing flow carries about 4.91 kW. Multiplying by the 0.92 design assumption would give a 4.52 kW shaft estimate. At 4 m, 5 kW requires at least 0.1385 m³/s with 92% efficiency. At the rounded candidate (3.60 m, 0.144 m^3/s), water power is about 5.09 kW and 5 kW shaft power would require 98.32% efficiency. If 34.61% were maintained at 3.60 m, the same target would require 0.409 m³/s. That last value is an energy-balance scenario, since the archived calculations do not show operation at this flow.

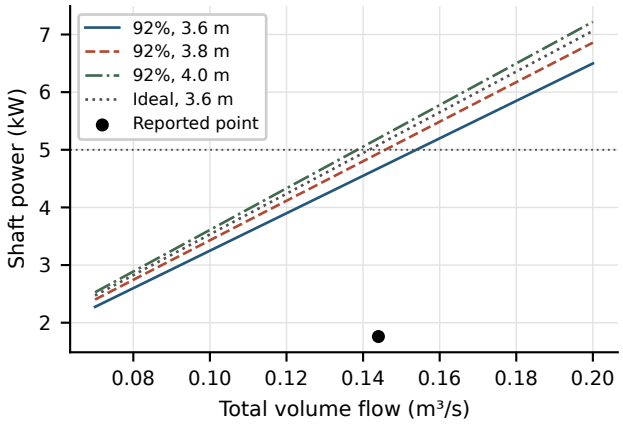

Figure 4.8 – Python. Conditional energy balances at three fixed heads and two assumed efficiencies. The archived 1.76 kW point is included for scale. These curves are not runner performance maps.

At the archived point, a pair of independent identical units would deliver about 3.52 kW if each saw the same head and discharge. Three would give about 5.28 kW under the same assumption and require approximately 0.432 m³/s in total. If a fixed total discharge is divided among parallel units at a common head, the total hydraulic input remains $\rho_w g Q_{total} H$. Efficiency and operating point may shift. Multiplying the number of machines alone cannot multiply the water energy of one fixed site.

5. Generator and converter modelling

5.1 Mechanical and electrical duty

The archived generator study uses a surface-mounted permanent-magnet synchronous machine. Its first sizing treats the cross-section as axially uniform, neglects end effects and approximates the yokes as high-permeability material. This permits a first calculation of induced EMF, torque, magnet thickness and current loading [1, 4]. The shaft power and speed that drive this calculation must belong to the same application case.

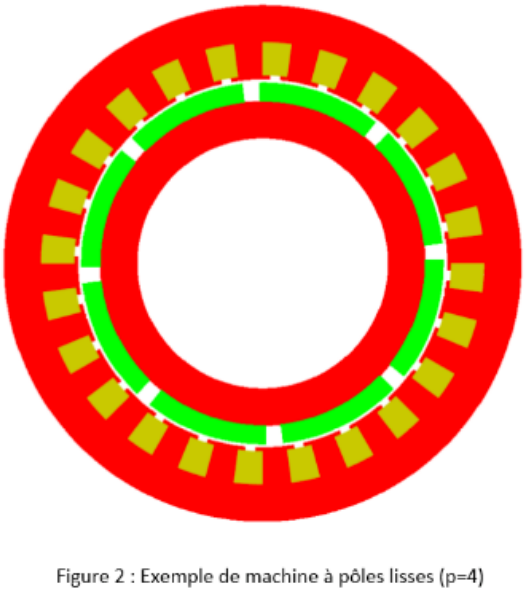

Figure 5.1 – Original machine cross-section used for preliminary electromagnetic sizing. Source Fig. 5.1, p. 21 of [1].

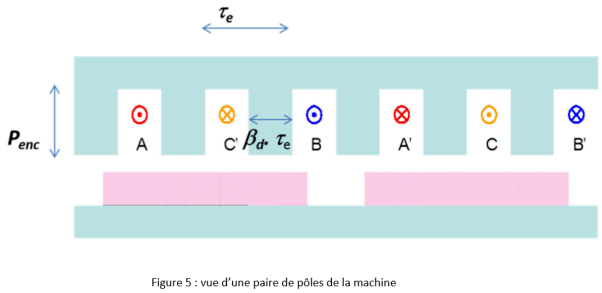

Figure 5.2 – Original drawing of outgoing and return conductors in the stator slots. Source Fig. 5.2, p. 21 of [1].

The mechanical and electrical angular speeds satisfy $\omega_e = p\omega_m$, where p counts pole pairs. The shaft relation $P_s = M\omega_m$ gives 11.21 N·m for 1.760 kW at 1500 rpm and 31.83 N·m for 5 kW at the same speed. The printed generator example states 152 N·m, corresponding to 23.88 kW at 1500 rpm. At 5 kW that torque corresponds to about 314 rpm. The source writes a division by the pole count in its nominal speed expression. That division is appropriate when converting electrical cycles per minute to mechanical angular speed. It must be omitted if the input is already shaft rpm. Without an identified nominal machine speed, winding data and loss budget, the 152 N·m example remains a separate sizing result.

5.2 Field, conductor EMF and mean torque

The constitutive approximations used in [1] are retained in (11). The symbol H_m denotes field intensity, distinct from net hydraulic head.

$$\begin{aligned} B &= \mu H_m, \qquad B_g = \mu_0 H_g \\ B_y &= \mu_0 \mu_r H_y, \\ B_a &= \mu_0 H_a + B_r. \end{aligned} \tag{11}$$

With stator-fixed azimuth θ and odd space harmonics of the surface-magnet field, one writes

$$B(\theta, t) = \sum_{k=0}^{\infty} B_{2k+1} \cos[p(2k+1)(\theta - \omega_m t)]. \tag{12}$$

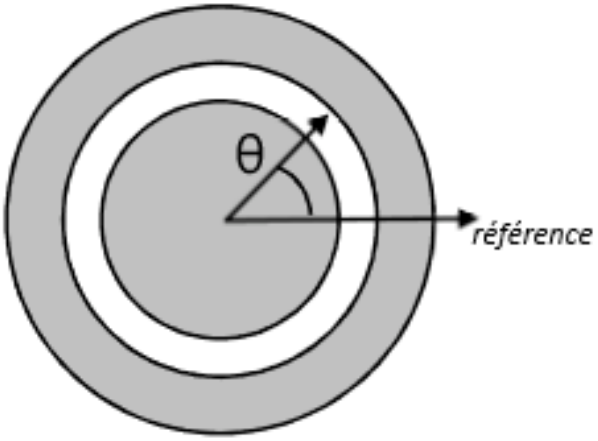

Figure 5.3 – Stator-fixed angular convention used in the original derivation. Source Fig. 5.3, p. 22 of [1].

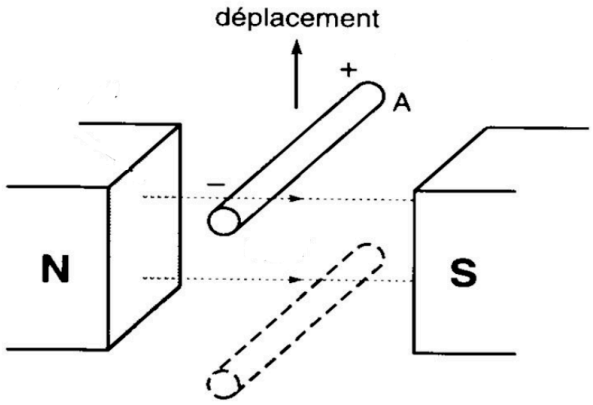

Figure 5.4 – Original flux-cutting diagram. Conductor and return-conductor polarities enter the signed phase EMF. Source Fig. 5.4, p. 22 of [1].

For a conductor of active length L swept at speed $v = \omega_m D/2$ across a radial field, the motional magnitude is BLv when the vectors are perpendicular. In the flat local approximation the swept flux is $\varphi = BLx$, so $d\varphi/dt = BLv$. A return conductor reverses the sign of the electrical contribution when separated by one electrical half-period. The mechanical spacing is π/p, giving the π/2 of [1] if the example uses two pole pairs. If n_c is the effective number of series active conductors per phase including any winding factor, the phase formula reads

$$\theta_i = \frac{2\pi(i-1)}{3p}, \quad i = 1,2,3$$
$$e_i(t) = n_c \frac{\omega_m D}{2} L B(\theta_i, t). \tag{13}$$

For balanced sinusoidal currents with phase RMS value I and angle ψ relative to the fundamental EMF, orthogonality of Fourier harmonics over an electrical period removes higher odd field harmonics from the mean product. Multiplication of cosines at the same frequency leaves a mean (cosψ)/2. The fundamental induction amplitude B_1 consequently enters the mean power explicitly.

$$E_1 = \frac{n_c B_1 L \omega_m D}{2\sqrt{2}}$$
$$\langle P_{em} \rangle = 3 E_1 I \cos\psi \tag{14}$$
$$\langle T_{em} \rangle = \langle P_{em} \rangle / \omega_m.$$

For the source linear loading and bore-volume conventions,

$$A_\ell = \frac{3 n_c I}{\pi D}, \qquad V_b = \frac{\pi D^2 L}{4}$$
$$\langle T_{em} \rangle = \sqrt{2} B_1 A_\ell V_b \cos\psi. \tag{15}$$

The printed intermediate mean-power line omits B_1. It is required both by the fundamental EMF expression and by dimensions. The final torque equation of [1] already contains it. For fixed current amplitude and voltage harmonics as assumed, the average torque is maximal at zero phase displacement. Non-sinusoidal current can contribute to torque ripple and, where matching harmonics are present, to the mean power.

5.3 Magnet thickness and fundamental induction

With air-gap length g_m, magnet thickness e_a, negligible current enclosed by the magnetic contour and equal effective cross-sectional areas, Ampère's law gives $2H_a e_a + 2H_g g_m = 0$. Continuity of normal induction and (11) then give the nominal flat-field value.

$$\widehat{B} = B_a = B_g, \qquad H_a e_a + H_g g_m = 0$$
$$X = \frac{\widehat{B}}{B_r} = \frac{e_a}{g_m + e_a}. \tag{16}$$

The simplified magnet law in (11) uses recoil permeability μ_0. Leakage, fringing, finite yoke reluctance, the actual magnet recoil line and saturation can change the result. For a rectangular induction of amplitude $\widehat{B}$ and symmetric pole-arc coverage β_p, where the coverage is a fraction of a pole pitch, Fourier integration of the positive and negative arcs gives

$$B_1 = \frac{1}{\pi} \int_{-\pi}^{\pi} B(\vartheta) \cos\vartheta \, d\vartheta$$
$$B_1 = \frac{4\widehat{B}}{\pi} \sin\left(\frac{\beta_p \pi}{2}\right). \tag{17}$$

Here ϑ is the electrical angle. The finite-arc result follows from twice the integral of the positive-field lobe and the equal contribution of the negative lobe. At $e_a = g_m$, X=0.5. At $e_a = 5 g_m$ it is about 0.833. The logarithmic sensitivity of X to thickness is $g_m/(g_m+e_a)$, explaining the declining gain per added thickness. Figure 5.6 applies (16) and (17) for three coverage assumptions. The result concerns the fundamental of the ideal waveform. Saturation and demagnetisation require material data.

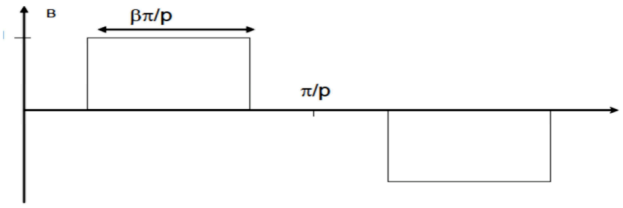

Figure 4 : forme d'onde de l'induction dans l'entrefer en fonction de ϑ dans le repère lié au rotor

Figure 5.5 – Original idealised radial air-gap waveform. Pole coverage fixes the support of the positive and negative field lobes. Source Fig. 5.5, p. 24 of [1].

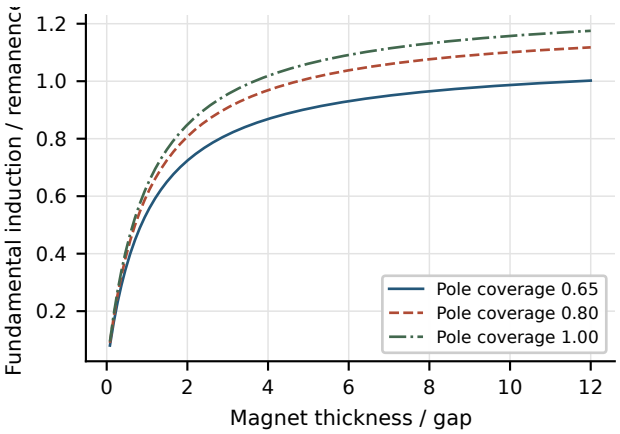

Figure 5.6 – Python. Normalised fundamental field from the gap and pole-arc model, using illustrative coverage fractions of 0.65, 0.80 and 1.00.

5.4 Active length and thermal scale

Combining (15)–(17) at ψ=0 simplifies the nominal active-length estimate to

$$T_{em} = \sqrt{2} A_\ell D^2 L X B_r \sin(\beta_p \pi/2)$$
$$L = \frac{T_{em}}{\sqrt{2} A_\ell D^2 X B_r \sin(\beta_p \pi/2)}. \quad (18)$$

The printed torque line lacks X, which appears again in the printed expression for L. Equation (18) uses a consistent substitution. Using the current density $J=I/S_c$ and conductor resistivity ρ_e, the ideal active-length copper loss is

$$k_r = \frac{\sum S_c}{S_{\text{slot}}}$$
$$P_J = 3 n_c \frac{\rho_e L}{S_c} I^2$$
$$= \rho_e \pi D L A_\ell J \quad (19)$$
$$\Delta T \sim \frac{P_J}{h_T \pi D L}$$
$$\sim \frac{\rho_e A_\ell J}{h_T}.$$

This approximation uses one representative convection coefficient and the cylindrical surface as heat-transfer area. It omits ends, core losses, contact resistances and temperature-dependent resistivity. The archived ranges J=3–7 A/mm² and A_ℓ=12–60 kA/m are screening inputs. Ratings would require magnet and yoke saturation, slot fill, pole count, electrical frequency, winding temperature and actual heat paths. The original simulation panels show a flux-density field, phase linkage and an angle-dependent torque trace. They do not identify a common thermal and mechanical nameplate for the hydraulic operating point.

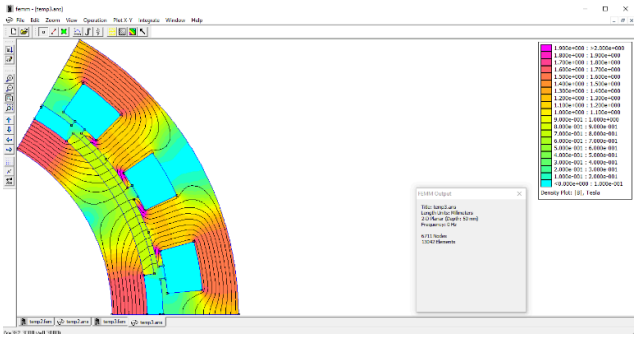

Figure 5.7 – Original FEMM flux-density result. The scientific window is cropped to retain the field and its scale. Source Fig. 5.6, p. 26 of [1].

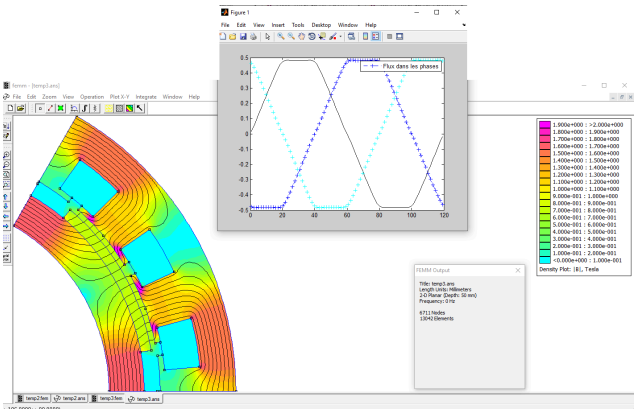

Figure 5.8a – Archived magnetic field and phase-linkage display. The same crop preserves the plots and scales while omitting background desktop content. Source Fig. 5.7a, p. 26 of [1].

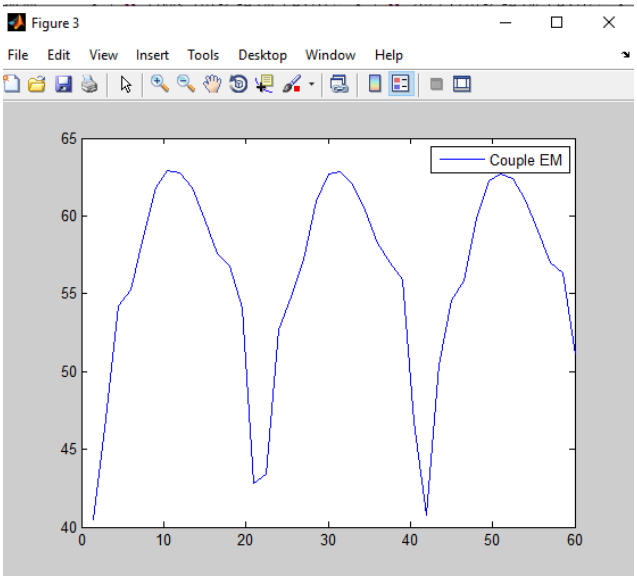

Figure 5.8b – Original electromagnetic torque plot, cropped to its plotting window. Source Fig. 5.7b, p. 26 of [1].

5.5 Variable-speed control structure

The archived speed-control simulation uses an outer speed regulator and inner current loops. With the source motor sign convention, the rotor equation is $J_m\dot{\omega}_m = T_{em} - T_L$. For generator operation a positive hydraulic torque and an opposing electrical torque can instead be written as $J_m\dot{\omega}_m = T_h - T_g - T_f$, where T_f denotes mechanical loss. The signs must be set before a plotted torque is interpreted as drive or braking.

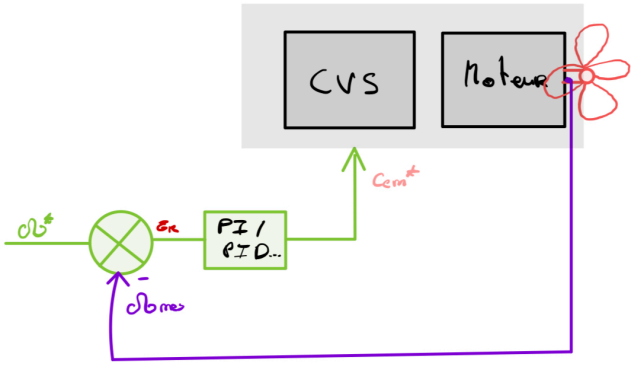

Figure 5.9 – Global original speed and converter architecture. Source Fig. 5.8, p. 27 of [1].

For $\theta_e = \omega_e t$ and phase offset $\gamma_i = 2\pi(i-1)/3$, the source sinusoidal-flux model is

$$\begin{aligned} \phi_i &= \sqrt{2}\,\phi_{\mathrm{rms}}\cos(\theta_e - \gamma_i) \\ e_i &= -\frac{d\phi_i}{dt} \\ &= \sqrt{2}\,\phi_{\mathrm{rms}}\omega_e \sin(\theta_e - \gamma_i) \\ P_e &= 3EI\cos\psi, \qquad T_{em} = P_e/\omega_m. \end{aligned} \tag{20}$$

The terminal relation $P = 3VI\cos\alpha$ uses phase RMS quantities and the terminal power-factor angle. It differs from the air-gap product with the back-EMF angle because current also creates voltage drops and energy storage terms.

The Park transformation maps the three measured currents into a synchronous frame. It makes ideal sinusoidal steady state constant in that frame, while speed-dependent electrical terms remain in the current dynamics [4]. For amplitude-invariant current variables and one common sign convention, the surface-magnet model is

$$\begin{aligned} v_d &= R_s i_d + L_d\dot{i}_d - \omega_e L_q i_q \\ v_q &= R_s i_q + L_q\dot{i}_q + \omega_e(L_d i_d + \lambda_m) \\ T_{em} &= \tfrac{3}{2}p[\lambda_m i_q + (L_d - L_q) i_d i_q]. \end{aligned} \tag{21}$$

For $L_d = L_q$ the reluctance-torque term vanishes. The cross-coupled voltage terms in (21) can be compensated in the inner loops. The converter still constrains the realised voltage. The archived current and speed responses illustrate the cascade. There is no recovered switching-project file or calibrated machine load trace for closed-loop quantitative comparison.

5.6 PWM waveform and R–L check

The source simulations compare an ideal sinusoidal three-phase supply and a switched voltage-source inverter using intersective PWM [5]. At nominal 50 Hz, the archived voltage spectra show clusters near the selected 2 kHz carrier and its multiples. A sinusoidal fundamental alone filters differently from a waveform that includes switching sidebands. The archived circuit uses $R_s = 10\ \Omega$ and writes $L = 0.001$ H together with 150 Hz and 1 ms. The correct single-pole relations are

$$\frac{I(j\omega)}{V(j\omega)} = \frac{1}{R_s + j\omega L} \tag{22}$$

$$\tau = \frac{L}{R_s}, \quad f_{-3\mathrm{dB}} = \frac{R_s}{2\pi L}.$$

For 1 mH the exact values here are 0.10 ms and 1591.55 Hz. For 10 mH they are 1.00 ms and 159.15 Hz. The source's approximately 150 Hz and 1 ms are therefore compatible with 10 mH. This matters because one original comparison changes the carrier from 2000 to 500 Hz while increasing the inductance from 1 to 10 mH. That comparison mixes two parameters.

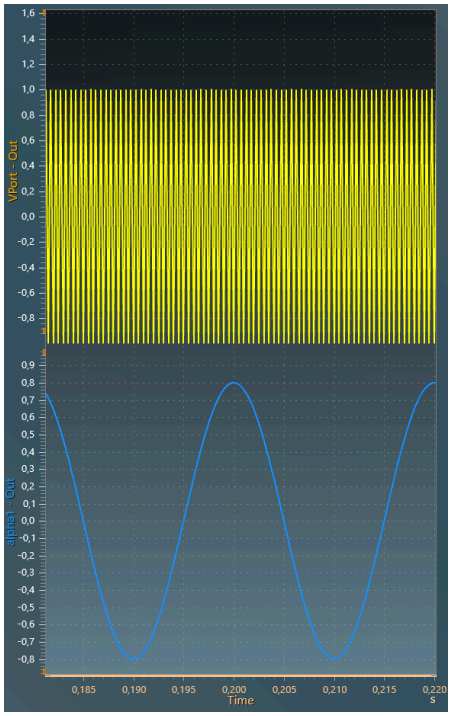

Figure 5.10 – Original ideal-supply and switched voltage waveforms. Source Fig. 5.9, p. 28 of [1].

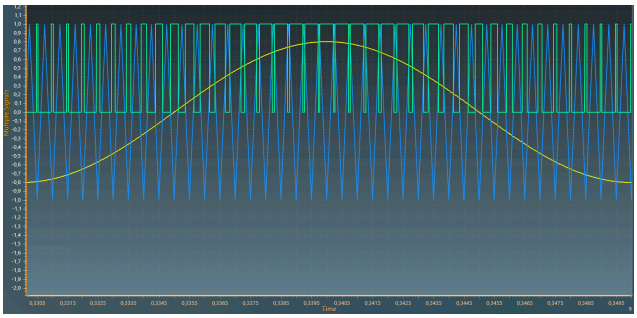

Figure 5.11 – Archived time-domain and spectral comparison of the source voltages. Source Fig. 5.10, p. 28 of [1].

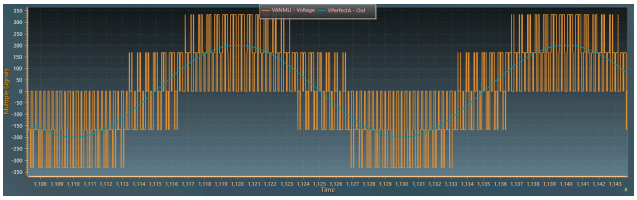

Figure 5.12 – Original PWM phase-voltage comparison with an ideal sinusoid. Source Fig. 5.11, p. 28 of [1].

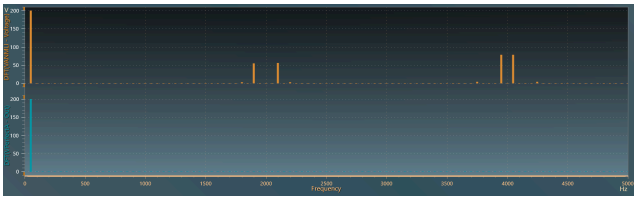

Figure 5.13 – Original converter output DFT. Switching groups are visible around the carrier harmonics. Source Fig. 5.12, p. 29 of [1].

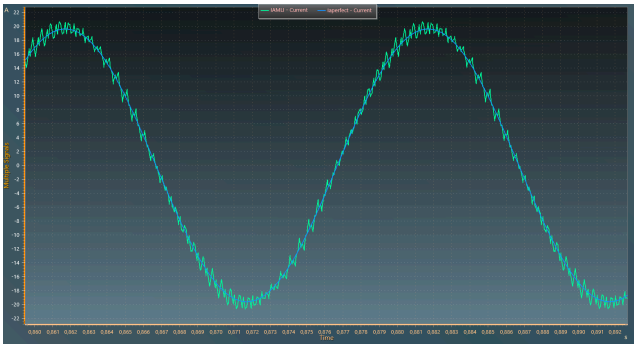

Figure 5.14 – Archived ideal and PWM-fed phase-current waveforms. Source Fig. 5.13, p. 29 of [1].

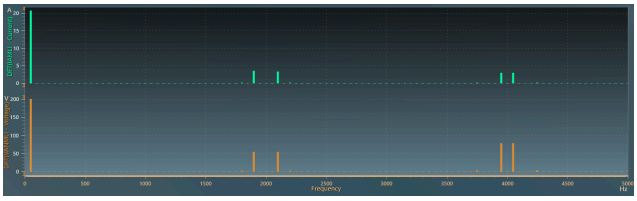

Figure 5.15a – Original changed-parameter current response. Source Fig. 5.14a, p. 30 of [1].

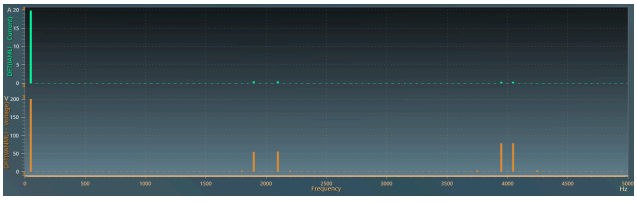

Figure 5.15b – Voltage response for the same archived comparison. Source Fig. 5.14b, p. 30 of [1].

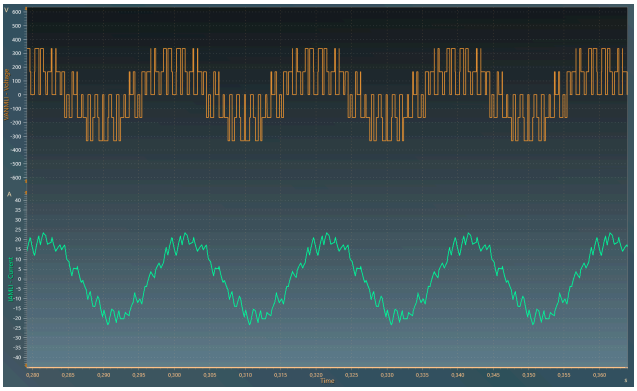

Figure 5.16 – Original comparison of converter configurations. Carrier and inductance are treated as separate factors in the added study. Source Fig. 5.15, p. 30 of [1].

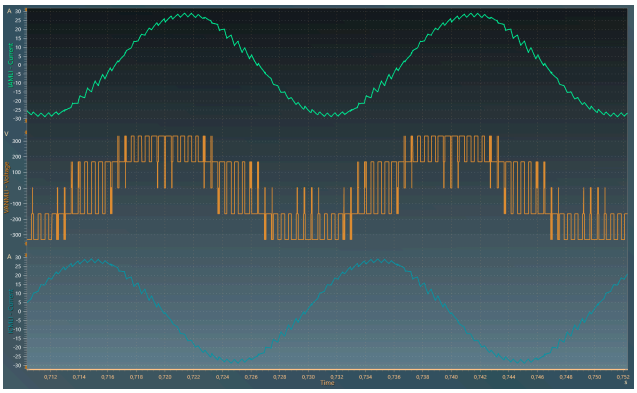

Figure 5.17 – Archived response after increasing the setting labelled maximum voltage to 350 V. The source setting is preserved on its original scale. Source Fig. 5.16, p. 31 of [1].

5.7 Independently switched three-phase test

The new calculation isolates the converter and a symmetric star-connected R–L load with a floating neutral. It assumes a 350 V DC link, modulation index 0.75 and 50 Hz sinusoidal references. These are explicit benchmark inputs. The archived 350 V value is a model limit and does not establish the physical DC voltage. The load has zero back-EMF in this calculation. Both carrier values (500 and 2000 Hz) are crossed with both inductances (1 and 10 mH). Each two-level pole state is the result of a sinusoid-to-triangle comparison. With s_k the binary state and $\bar{s}=(s_a+s_b+s_c)/3$,

$$\begin{aligned} v_k &= V_{dc}(s_k-\bar{s}), \qquad L\dot{i}_k + R_s i_k = v_k \\ i_k(t+\Delta t) &= e^{-R_s\Delta t/L} i_k(t) \\ &+ \frac{1-e^{-R_s\Delta t/L}}{R_s} v_k(t). \end{aligned} \tag{23}$$

The exact R–L transition uses voltage held over each numerical interval. The switch decisions are sampled at the midpoint. Five steady cycles sampled at 0.5 µs are used for RMS and Fourier calculations after a 0.10 s transient interval. The corresponding ideal sinusoidal baseline has RMS fundamental voltage $mV_{dc}/(2\sqrt{2})$. Current-THD is the ratio of residual RMS current after separating the DC and fundamental terms, to the RMS fundamental. The scalar test checks neutral current closure and the fundamental impedance relation in all cases. Halving the step from 1.0 to 0.5 µs changes phase-A THD by at most 0.039 percentage point.

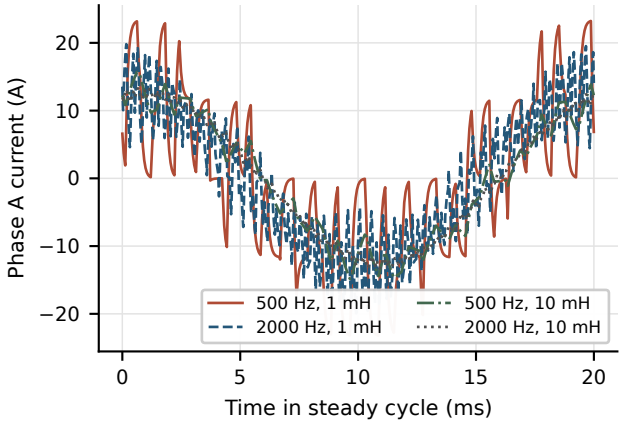

Figure 5.18 – Python. Phase-A current over one steady electrical period for the four benchmark combinations.

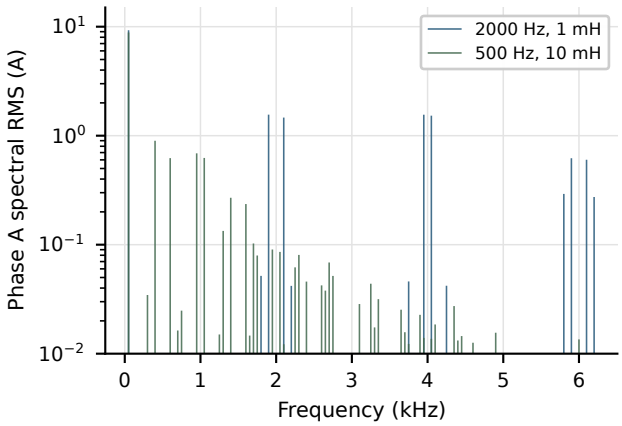

Figure 5.19 – Python. Phase-A harmonic groups for the two combinations used in the source parameter change. The 50 Hz fundamental is retained.

Table 5.1 – Switched three-phase R–L benchmark at 50 Hz. Current and THD describe phase A. The harmonic dissipation is summed over the three model resistors.

Carrier (Hz)	L (mH)	Cut-off (Hz)	I_1 RMS (A)	THD (%)	Harmonic loss (W)
500	1	1591.55	9.276	73.87	1409.92
2000	1	1591.55	9.278	35.09	318.04
500	10	159.15	8.854	17.04	68.29
2000	10	159.15	8.855	4.27	4.30

With 1 mH at 2000 Hz, the model gives about 35.09% phase-A current THD. The 500 Hz and 10 mH combination gives about 17.04%, confirming that added inductance can more than offset a lower carrier in this benchmark. At fixed inductance, increasing the carrier improves current waveform quality in the tested cases. At 10 mH, 2000 Hz gives about 4.27% THD. The tabulated three-phase harmonic dissipation is calculated as $R_s \sum_k I_{k,h}^2$ for this ideal R–L load. It quantifies filtering in the benchmark and cannot be directly applied to generator copper loss or converter efficiency. Semiconductor losses would require a device model, switching transitions, current and temperature.

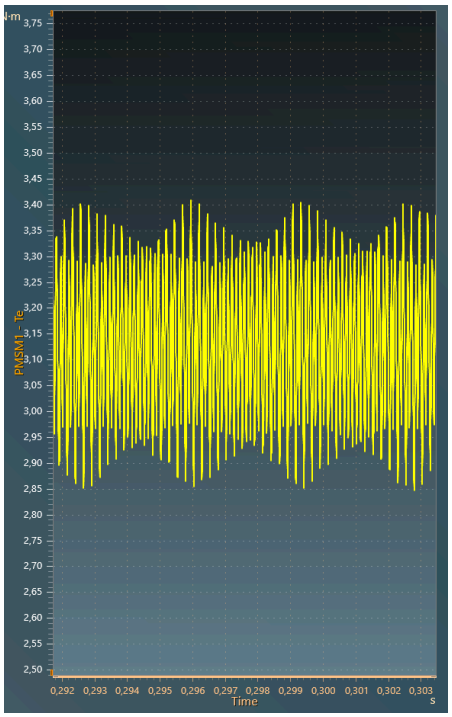

Figure 5.20a – Original time trace from the torque-model comparison. Source Fig. 5.17a, p. 31 of [1].

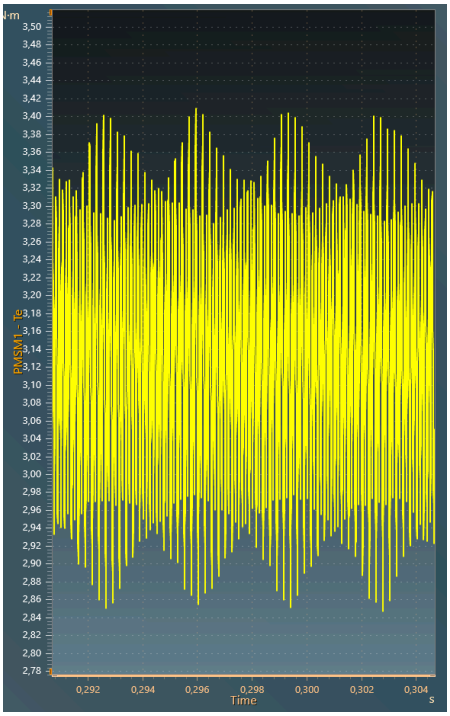

Figure 5.20b – Original torque response at zero current-to-EMF displacement. Source Fig. 5.17b, p. 31 of [1].

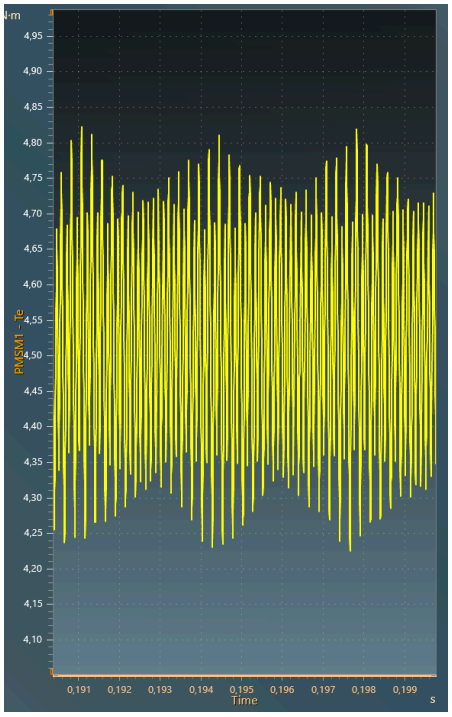

Figure 5.20c – Response panel associated with the 45° and 90° tests in [1]. Source Fig. 5.17c, p. 31 of [1].

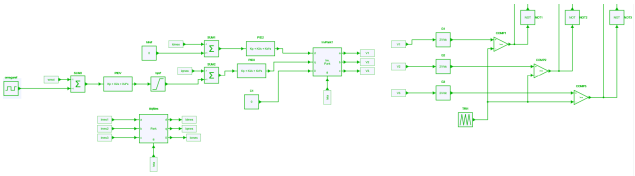

Figure 5.21a – Original modulation and reference-frame transformations. Source Fig. 5.18a, p. 31 of [1].

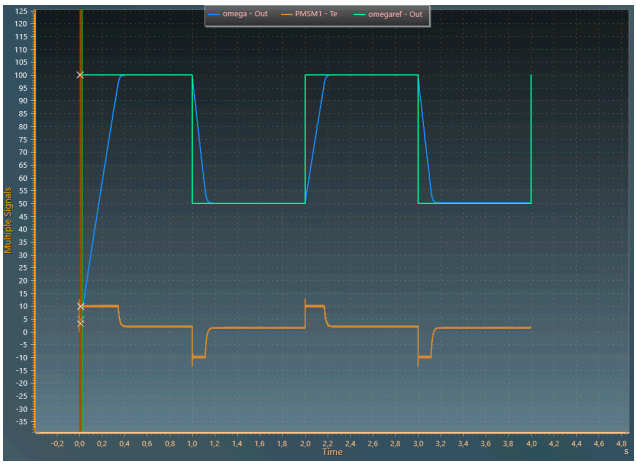

Figure 5.21b – Original speed command, simulated speed and electromagnetic torque in the regulation sequence. Source Fig. 5.18b, p. 31 of [1].

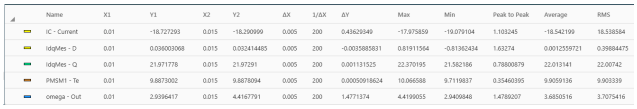

	Name	X1	Y1	X2	Y2	ΔX	1/ΔX	ΔY	Max	Min	Peak to Peak	Average	RMS
	IC - Current	0.01	-18.727293	0.015	-18.290999	0.005	200	0.43629349	-17.975859	-19.079104	1.103245	-18.542199	18.538584
	IdqMes - D	0.01	0.036003068	0.015	0.032414485	0.005	200	-0.0035885831	0.81911564	-0.81362434	1.63274	0.0012559721	0.39884475
	IdqMes - Q	0.01	21.971778	0.015	21.97291	0.005	200	0.001131525	22.370195	21.582186	0.78800879	22.013141	22.00742
	PMSM1 - Te	0.01	9.8873002	0.015	9.8878094	0.005	200	0.00050918624	10.066588	9.7119837	0.35460395	9.9059136	9.900339
	omega - Out	0.01	2.9396417	0.015	4.4167791	0.005	200	1.4771374	4.4199055	2.9409848	1.4789207	3.6850516	3.7075416

Figure 5.22 – Original numerical statistics for the simulated speed, torque and current signals. Source Fig. 5.19, p. 32 of [1].

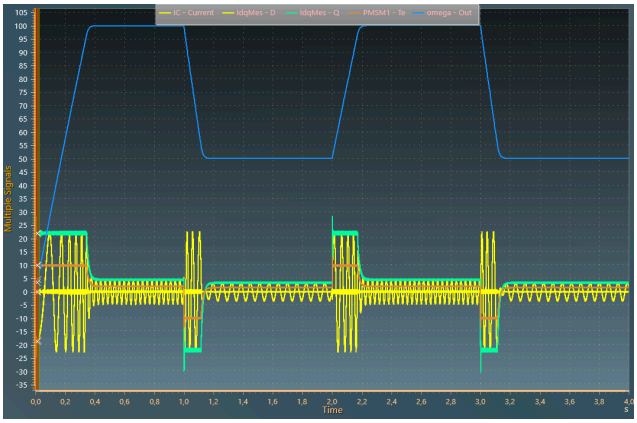

Figure 5.23 – Original traces of current references and measured components in the simulation. Source Fig. 5.20, p. 32 of [1].

The torque plot during accelerations indicates temporary demand above the later steady value. The negative torque portions align with the braking phases under the source convention. These original traces establish the model sequence and the signal meanings. They do not determine torque margin for the hydraulic rotor without consistent shaft speed, conversion losses and allowable phase-current and voltage conditions.

6. Prototype and wind-tunnel experiment

6.1 Manufacture and test configuration

The CAD runner was sliced in PrusaSlicer and made by fused-filament fabrication. The archive identifies PLA, extrusion around 200 °C, support generation and removal. It also contains a 20 µm value described as filament diameter. The figure record does not identify that setting, so it is retained as reported and is not used to infer filament feed, layer height or tolerances. The post-processed specimen provides a physical check of printability and rotation in the tunnel.



Figure 6.1a – Original photograph of the runner on the build plate. Source Fig. 6.1a, p. 33 of [1].

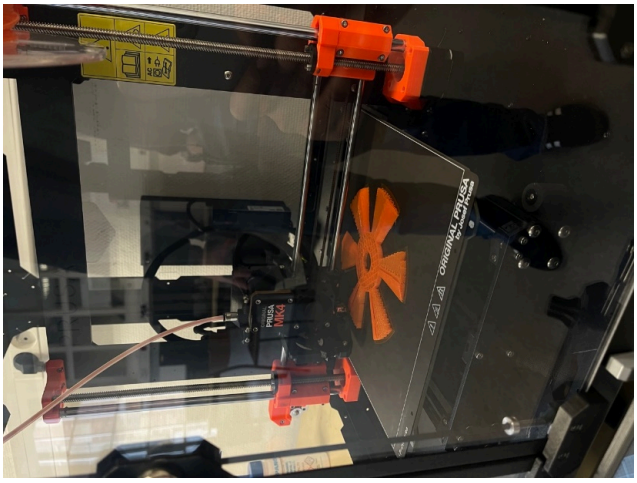

Figure 6.1b – Original image of the prototype during manufacture. Source Fig. 6.1b, p. 33 of [1].

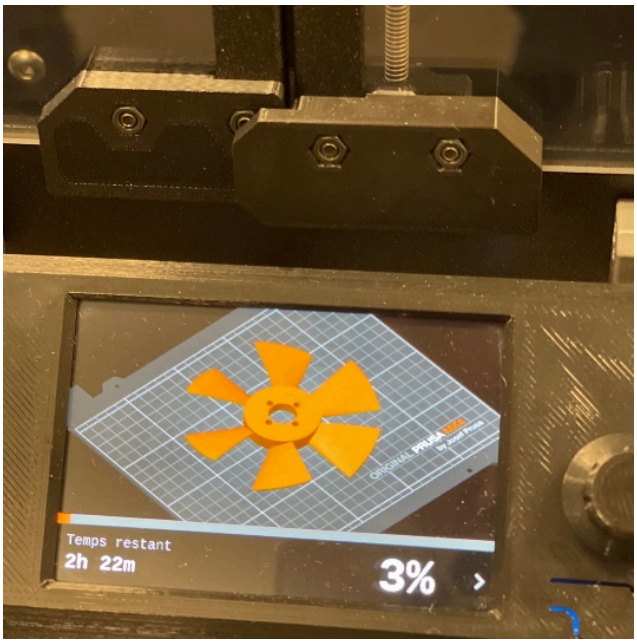

Figure 6.1c – Original printer display and monitored build. Source Fig. 6.1c, p. 33 of [1].

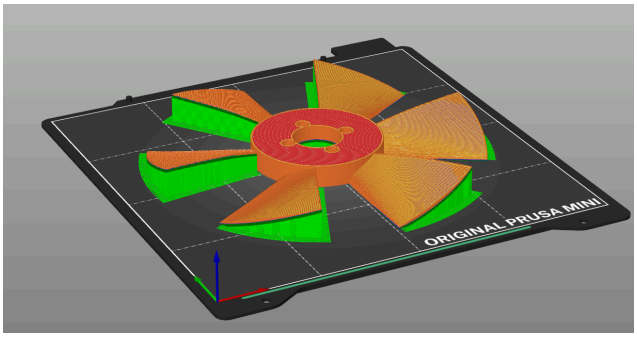

Figure 6.2 – Archived sliced geometry and support generation. Source Fig. 6.2, p. 33 of [1].

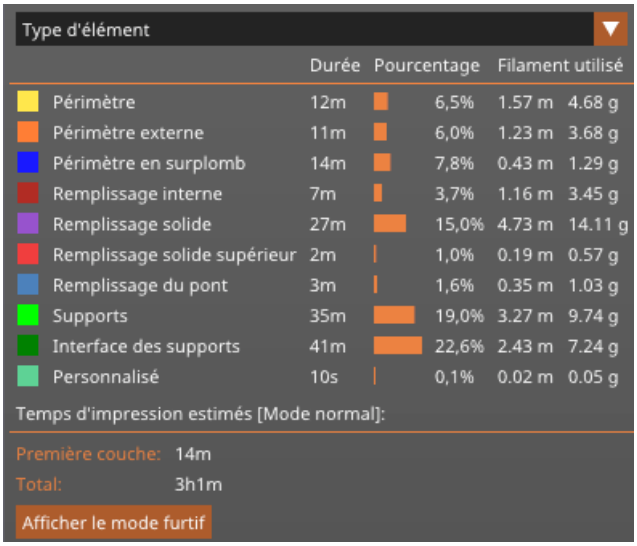

Figure 6.3a – Original slicer display with the print-time and material breakdown. Source Fig. 6.3a, p. 34 of [1].

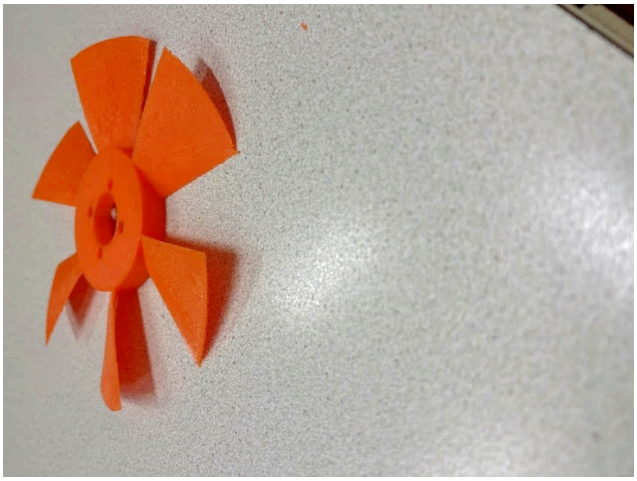

Figure 6.3b – Side view of the printed runner. Source Fig. 6.3b, p. 34 of [1].



Figure 6.3c – Post-processed turbine prototype. Source Fig. 6.3c, p. 34 of [1].

The prototype was installed in a semi-guided test section of a recirculating wind tunnel. The source describes a maximum tunnel velocity around 40 m/s and a contraction ratio around 12.5. Its statement of about 10% turbulence applies to a return-valve region and does not identify testing-section turbulence. Tunnel-blockage correction, tip clearance relative to the setup, balance calibration, resolution of the torque samples and actual air properties are unavailable. The photos and schematic document the arrangement.

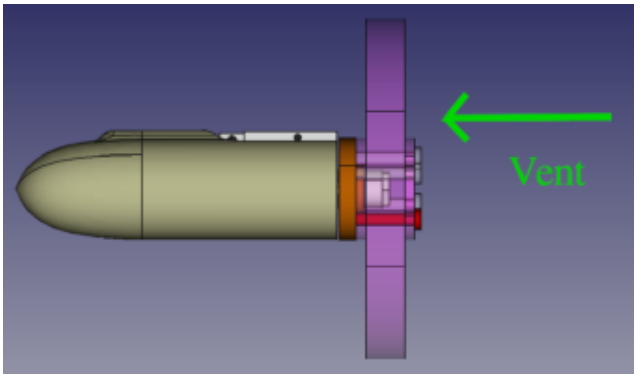

Figure 6.4 – Original CAD view of the tunnel configuration, with the indicated flow direction. Source Fig. 6.4, p. 34 of [1].

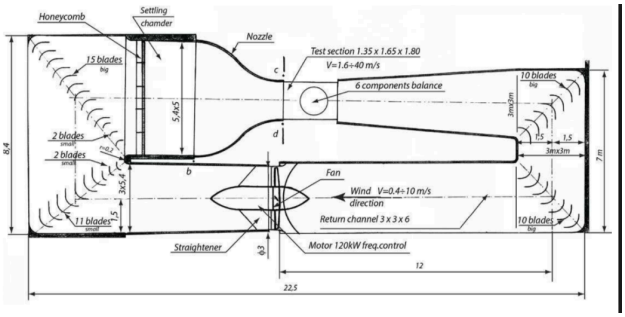

Figure 6.5 – Archived facility schematic, showing the recirculation and test section. Source Fig. 6.5, p. 36 of [1].



Figure 6.6a – Original photo of prototype and instrumentation. Source Fig. 6.6a, p. 36 of [1].



Figure 6.6b – Second archived view of the installed equipment. Source Fig. 6.6b, p. 36 of [1].

6.2 Reconstructed aerodynamic point

The first experiment in [1] varies rotational speed at a stated wind speed of 10 m/s. It uses a disc radius of 75 mm and assumed density of 1.2 kg/m³. With $S=\pi R_a^2$, torque C and ω_a the mechanical speed, the source power coefficient and tip-speed ratio are

$$\begin{aligned} P_s &= C\omega_a, \quad U = R_a\omega_a, \quad \lambda = U/V \\ P_{\text{air}} &= \tfrac{1}{2}\rho_a S V^3, \quad C_p = P_s/P_{\text{air}} \\ C_Q &= \frac{C}{\tfrac{1}{2}\rho_a S V^2 R_a} \\ &= \frac{C_p}{\lambda}. \end{aligned} \tag{24}$$

The Pitot-type conversion in the source is $V=\sqrt{(2\Delta\, p/\rho_a)}$ when the measured pressure difference is the dynamic pressure. At $\omega_a=190.5$ rad/s and $C_p=0.239$, the stated quantities imply $\lambda=1.42875$, incoming kinetic power of 10.603 W, shaft power of 2.534 W and torque of 0.01330 N·m. The corresponding torque coefficient is 0.1673. These are derived estimates at one reported point. They are not independent measured values.

A second series varied wind speed. Source [1] describes an approximately linear power trend over

the tested range and a maximum efficiency of approximately 0.56. It supplies no tabulated series, uncertainty values or denominator to establish that efficiency on the same basis as C_p. If the same rotor-disc kinetic power is used as denominator, the efficiency is the power coefficient by definition. The two reported maxima therefore require clarification of the operating points and normalisations. Neither is used as a water-turbine efficiency. Figure 6.7 compares model scalings through the one recoverable point.

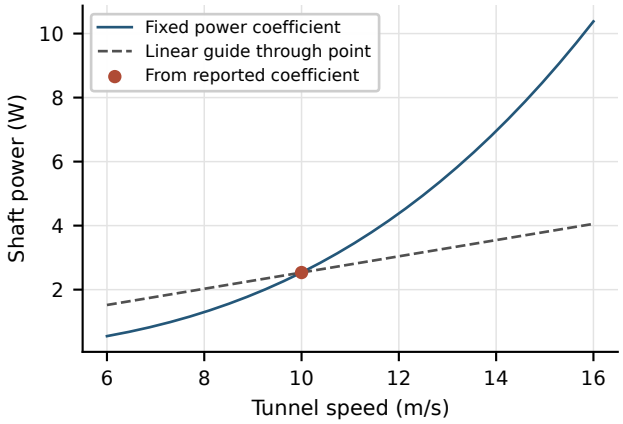

Figure 6.7 – Python. A cubic continuation at fixed power coefficient and a linear guide, both through the point inferred from the reported coefficient. No additional air measurements are generated.

At fixed geometry and density, P V^3 only if C_p stays fixed. If power were proportional to V over an interval, this would imply C_p V^{-2} on the disc basis. Changes in speed control and tip-speed ratio can change C_p during such a sweep. Without speed and torque histories, the apparent slope cannot be attributed to a scaling regime.

6.3 Transfer limits

For comparison, use the axial Reynolds number $Re_D=VD/\nu$, with runner diameter D and kinematic viscosity ν. For the air case, V=10 m/s, D=0.150 m and an assumed $\nu=1.5\times10^{-5}$ m²/s give about 1.0×10^5. For the nominal water model, $V=C_a=4.618$ m/s, D=0.206 m and an assumed $\nu=10^{-6}$ m²/s give about 9.51×10^5. The water tip-speed ratio on that axial velocity is about 3.50, compared with 1.43 in air. These are diameter-based comparisons. Blade-chord Reynolds number and blockage would use local velocities, chords and the actual surrounding flow area.

With the same air-scale diameter and viscosity assumptions, an air speed of about 95 m/s would match the water case's axial diameter Reynolds number, above the 40 m/s facility rating reported in [1]. Matching Reynolds number alone would still leave speed ratio and other similarity parameters to control. The tunnel test therefore establishes rotation and a recoverable torque signal in its own conditions. Hydraulic model performance requires matched conditions and instrumented water-side head and flow. The structured treatment of model-test quantities and scale effects in IEC 60193 [6] provides context for the distinction.

The measured wind speed has a cubic effect on the coefficient denominator. At a fixed measured shaft power a ±3% scaling error in V would shift an inferred 0.239 to roughly 0.219–0.262. This range follows from a specified calibration perturbation. In a repeat experiment the velocity, torque, rpm, density and tare should be measured together, with the same radius definition for every point. The magnitude of the shaft powers here also makes a friction or generator tare especially relevant.

7. Industrial scenario and sensitivity

7.1 Product and regional scope

The industrial work stream in [1] assumes a modular bulb-turbine product for low-head sites. Its reference unit is rated at 2 MW, with stated head range 1.5–10 m, peak efficiency assumption 85–90%, nominal cost EUR 2 million and 30–40 year design-life assumption. This is a separate MW-scale engineering and commercial scenario. At 3.6 m and assumed efficiency 87.5%, hydraulic power balance alone requires about 64.7 m³/s per 2 MW unit. The compact runner's design flow is about 0.132 m³/s. The scenario needs site

flow-duration data and its own geometry, loads and generator rating.

Critères	Auvergne-Rhône-Alpes	Occitanie	Grand Est	Nouvelle-Aquitaine	PACA
Potentiel hydraulique	9/10 (65 TWh/an)	7/10 (45 TWh/an)	6/10 (35 TWh/an)	8/10 (50 TWh/an)	**8/10 (45 TWh/an, +20 % prévu)**
Densité industrielle	8/10 (20 000 entreprises industrielles)	6/10 (12 000)	7/10 (15 000)	5/10 (10 000)	7/10 (15 000)
Réseaux logistiques	9/10 (2 ports, 1 aéroport, 5 lignes TGV)	7/10 (1 port, 1 aéroport, 2 lignes TGV)	8/10 (2 ports, 1 aéroport, 4 lignes TGV)	7/10 (1 port, 1 ligne TGV)	**9/10 (3 ports, 2 aéroports, 2 lignes TGV)**
Main-d'œuvre qualifiée	8/10 (Université Grenoble-Alpes, INSA Lyon)	6/10 (Université de Toulouse)	7/10 (Université de Strasbourg)	6/10 (Université de Bordeaux)	**7/10 (Université Aix-Marseille)**
Subventions potentielles	7/10 (5% réduction fiscale)	9/10 (8%)	6/10 (4%)	8/10 (6%)	**8/10 (6%, soutien fort aux énergies renouvelables)**
Impact environnemental	6/10 (Zones sensibles, contraintes élevées)	7/10 (Moins de pression)	5/10 (Zones protégées)	6/10 (Zones touristiques)	**7/10 (Zones sensibles, mais projets adaptés)**
Coût du terrain	7/10 (100 €/m² en moyenne)	8/10 (80 €/m²)	6/10 (120 €/m²)	7/10 (90 €/m²)	6/10 (150 €/m²)
Score total	**54/70**	50/70	45/70	47/70	**52/70**

Figure 7.1 – Original regional comparison. Its weights, resource figures and scores are scenario assumptions reported in [1]. Source Fig. 7.1, p. 38 of [1].

The original scenario selects Provence-Alpes-Côte d'Azur (PACA) using summer demand, water resource, infrastructure programmes, logistics and potential economic effects. The printed unweighted table gives Auvergne-Rhône-Alpes 54/70 and PACA 52/70. The selection therefore needs an explicit preference for factors such as logistics or seasonal demand. The archived projections, including the assumed regional investment exceeding EUR 50 million annually, are inputs to the original scenario.

Type de Turbine	Conditions d'utilisation	Efficacité	Coût (€/kW installé)	Adaptabilité aux projets PACA	Avantages principaux	Inconvénients
Kaplan	Faibles hauteurs de chute (<30 m) et débits élevés	90-95 %	1 200 - 2 000	Excellente	Haut rendement avec des débits variables	Plus complexe à installer et à maintenir
Pelton	Grandes hauteurs de chute (>100 m) et débits faibles	85-90 %	1 500 - 2 500	Faible	Idéale pour les régions montagneuses	Non adaptée aux faibles hauteurs de chute
Francis	Hauteurs de chute modérées (30-300 m), débits variés	80-90 %	1 000 - 1 800	Modérée	Bonne polyvalence pour des conditions variées	Moins efficace pour les très faibles hauteurs
Bulbe	Très faibles hauteurs de chute (<15 m) et débits élevés	80-85 %	1 800 - 2 500	Modérée	Idéale pour les zones avec très faibles pentes	Rendement inférieur à celui des Kaplan
Vis d'Archimède	Très faibles hauteurs de chute et débits très faibles	70-80 %	2 500 - 3 000	Faible	Simplicité de conception	Rendement faible, adapté uniquement aux microcentrales

Figure 7.2 – Original technology comparison. Its assumed operating ranges and costs apply to the industrial scenario. Source Fig. 7.2, p. 40 of [1].

Critère	Turbine Kaplan (grande capacité)	Petites turbines (Kaplan compactes, Bulbe, etc.)
Coût initial	Élevé (1 200 - 2 500 €/kW)	Faible à modéré (500 - 1 500 €/kW)
Maintenance	Optimisée avec technologies modernes	Maintenance accrue avec plusieurs unités
Rendement	90-95 %	75-85 %
Modularité	Faible	Excellente
Durée de vie	Longue (40-50 ans)	Modérée (20-30 ans)
Impact environnemental	Moyen	Faible
Adaptation aux débits	Meilleure pour grands débits	Meilleure pour faibles débits

Figure 7.3 – Original comparison of large Kaplan installations and smaller modular turbines. Source Fig. 7.3, p. 40 of [1].

Caractéristique	Valeur ou Plage Typique
Hauteur de chute nominale	1,5 m à 10 m
Débit optimal	5 m^3/s à 100 m^3/s
Puissance installée	100 kW à 3 MW (par unité)
Rendement maximal	85-90 %
Type de régulation	Régulation simple, avec palettes fixes ou ajustables
Durée de vie	30-40 ans (avec maintenance régulière)
Dimensions compactes	Installation intégrée dans des conduits ou canaux existants
Matériaux	Acier inoxydable et alliages résistants à la corrosion
Technologie additionnelle	Surveillance numérique pour le contrôle à distance et maintenance prédictive

Figure 7.4 – Original bulb-turbine concept and its assumed commercial characteristics. Source Fig. 7.4, p. 41 of [1].

The selection argument is suitability for low head, variable high discharge and modular placement. Kaplan concepts can vary blade pitch and guide flow, but the source's 90–95% institutional efficiency range is a comparison

assumption in the selection matrix. It is not transferred to the test runner or used to calculate the recovered hydraulic efficiency in Section 4.

7.2 Fleet energy and production schedule

At 2 MW and 6000 full-load-equivalent hours per year, a unit yields 12 GWh/year. The annual energy target of 2 TWh then requires 167 units. The assumed hours imply a capacity factor of 68.5% on an 8760 h year. Full-load-equivalent hours are an integral performance input combining water availability, head variation, derating and downtime. They are not necessarily hours energised.

$$E_y = P_u h_{\mathrm{FL}},$$
$$n_u = \left\lceil \frac{E_{\mathrm{goal}}}{P_u h_{\mathrm{FL}}} \right\rceil. \tag{25}$$

Données	2025	2026	2027	2028	2029
Prévisions de vente (unités)	33	66	99	133	167
Nombre d'unités produites (unités)	33	66	99	133	167
Stock final (unités)	33	33	33	34	34
Stock de sécurité (unités)	3	7	10	13	17

Figure 7.5 – Original sales, production and safety-stock chart. The 33/33/33/34/34 series is the annual production target in the text, and 33/66/99/133/167 is cumulative. Source Fig. 7.5, p. 41 of [1].

Table 7.1 – Original planning path and implied mature run-rate energy at 6000 equivalent hours. The forecast years are retained from the original study.

Planning year	Annual units	Cumulative	Energy (GWh/y)	Safety stock
2025	33	33	396	3
2026	33	66	792	7
2027	33	99	1,188	10
2028	34	133	1,596	13
2029	34	167	2,004	17

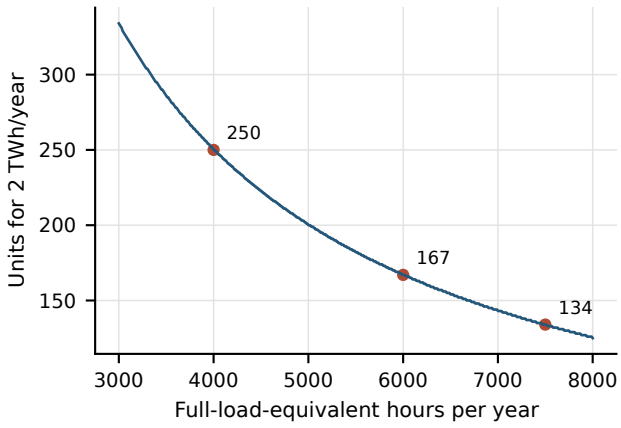

Figure 7.6 – Python. Fleet count required for a rated annual 2 TWh at the assumed 2 MW per unit, varied over full-load-equivalent hours.

The target falls to 134 units at 7500 equivalent hours and increases to 250 at 4000 hours. The archived year's cumulative energy columns indicate run-rate energy from the installed fleet once fully available. They are not partial-year generation during staggered commissioning. A five-year total of 167 sold turbines uses 3340 t of stainless steel at 20 t per turbine, matching about 167 t each quarter on average. If the 17-unit end stock is an additional fully completed reserve, producing that reserve requires 184 units in all, 340 t more steel and EUR 34 million of unit manufacturing cost at the original price basis. This is additional inventory and cash tied up, with its final financial treatment depending on whether units are sold or held.

7.3 Takt, lead time and event model

The original manufacturing plan specifies pre-assembly, final integration, coating and testing. The manufacturing bill of materials includes runner, casing, shaft, ten blades, bearings, generator, sensors and auxiliaries, including a nominal 20 L of lubricant. The plan assigns five CNC resources, three assembly stations and two paint booths, plus final acceptance. It also describes five line positions and two operating teams. These labels alone do not establish which resources can work simultaneously. Its staffing table lists 20 machining, 30 assembly, 10 coating and 10 quality-control operators, summing to 70 versus an indicated total of 85. An earlier

planning assumption gives about 60. Direct station times 50, 40, 20 and 10 hours sum to 120 hours, whereas the MRPII description also mentions 150 hours per turbine. The remaining 30 hours are not allocated to a named modelled activity.

On the source four-week accounting month, one resource contributes 140 working hours. If two teams add their labour hours, 280 h spread across a demand of three units corresponds to 93.33 team-hours per unit. This is not a chronological completion time. Serial lead time can exceed the planned completion interval in a pipeline. Capacity depends on where work overlaps and which resources are shared. The model uses the listed 120 hours as resource occupation durations, and defines a planning year as 12 × 140 working hours. The separate 220-day calendar would give 1540 h at 7 h/day. It is not mixed into the 1680-hour model year.

The event simulation releases the source's annual orders evenly through each year and starts with no work in progress. At each operation, the next eligible job starts when the earliest identical station can receive it. If a_j is arrival, b_m the selected station's availability and s_i the operation time, then

$$t_{j,i} = \max(a_j, b_m) + s_i, \qquad a_{j,i+1} = t_{j,i}. \tag{26}$$

The comparison uses three named resource scenarios. The declared station case takes 5/3/2/1 resources in machining, assembly, coating and testing. One final test station is an analysis assumption. A second case uses one independent station at each stage. A third uses two pooled teams, each assigned an entire 120 h unit through to completion. Shift calendars, batch setups, rework and supplier delays are omitted. These resource models test the source's different interpretations of parallelism.

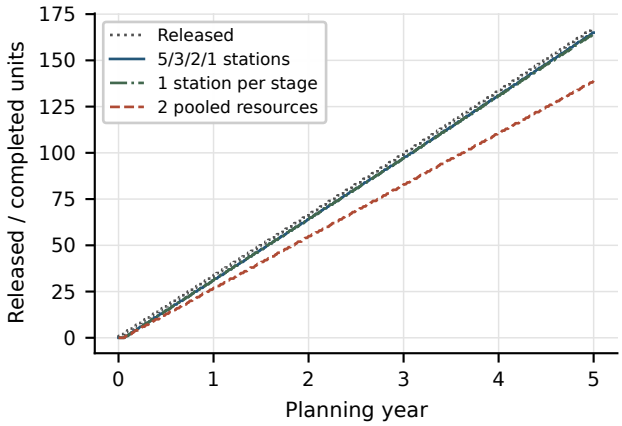

Figure 7.7 – Python. Cumulative release and completion in the three deterministic resource scenarios, starting empty. The source annual release counts are unchanged.

Table 7.2 – Deterministic capacity check. Production uses a 1680 h working-year clock. Lead time runs from job release to completion.

Resources	Year 1 done	Year 5 done	Year 5 open	Max. lead (h)
5/3/2/1 stations	31	165	2	120.0
One per stage	31	164	3	159.4
Two pooled teams	27	139	28	1729.4

The declared-station model completes 165 units by the year-five boundary, with two releases still inside their nominal 120 h flow time. The one-station-per-stage case finishes 164 and builds a small queue as the rate reaches 34 units per year. Two pooled teams finish 139, with 28 remaining and substantially larger lead times. With only two pooled resources the steady capacity is 2 × 1680/120 = 28 units per planning year. Lead-time and shipment targets require explicit calendar, workstation and inventory definitions. The schedules in the model are conditional checks and give no estimate of labour or delivery uncertainty.

7.4 Sourcing, cost reconciliation and finance

The archived industrial proposal retains runner and blade fabrication internally and buys casings, generators and specialist controls. It keeps lubrication integration and final acceptance with the assembly team. The location matrix compares France, Poland, Turkey, China and Portugal on capability, cost and distance. The chosen sourcing

case assumes critical machining in France and selected external supply in Poland or Turkey. The approximate cost basis changes from EUR 2.5 million per locally manufactured unit to EUR 2.0 million per mixed-sourcing unit, subject to qualification and logistics. It allocates EUR 0.8 million to machining, 0.6 million to assembly, 0.4 million to electrical systems and 0.2 million to treatment and quality. The archived sourcing and country tables appear in Appendix B.

The commercial assumptions are EUR 3 million selling price and EUR 2 million manufacturing cost for each of 167 units, plus EUR 30 million initial R&D and EUR 50 million fixed costs over five years. Total revenue is EUR 501 million and total cost EUR 414 million. The surplus is EUR 87 million, which gives 21.01% on the stated cost denominator. The 21.5% printed in [1] does not follow from those totals. The source payback convention treats the whole EUR 80 million burden as a fixed initial recovery amount and divides it by annual unit margin around EUR 33 million, yielding 2.42 years. It is a static calculation based on the stated definitions.

The Python case uses a separate cash timing convention. R&D is incurred at year zero, fixed costs are EUR 10 million each operating year, and annual receipts and production costs occur at year end for the original sequence. With price p_s, unit cost c_u, discount rate r_d and annual sales n_t, the cash flow is

$$V_0 = -30 + \sum_{t=1}^{5} \frac{(p_s - c_u)n_t - 10}{(1 + r_d)^t}. \tag{27}$$

All values are in EUR million. At a modelled 8% rate, value is EUR 63.25 million at 2.0 million per unit, EUR 23.30 million at 2.3 million and EUR −16.66 million at 2.6 million. The break-even unit cost for this defined case is about EUR 2.475 million. The inputs are source assumptions and sensitivity values. No financing, tax, warranty, working capital, installation or inventory value is included.

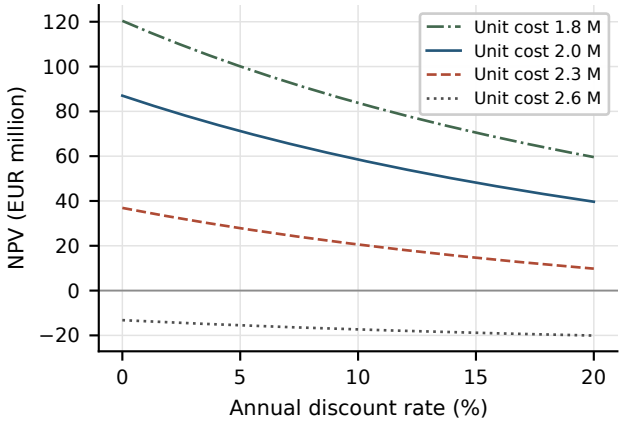

Figure 7.8 – Python. Present value under four assumed unit costs with original quantities, fixed cash-flow timing and a variable discount rate.

The MW-class energy, operations and cash-flow analyses together locate the key premises of the industrial scenario. A plant-level review would require contracted head and flow duration, permitting, delivered and installed cost, capacity and acceptance tests. The model's role is to identify which cost and staffing assumptions drive the result under fixed selling prices and orders.

8. Conclusions

The archived 3.8 m duty point and five-station MATLAB velocity triangles are reproducible from the sizing assumptions, including the hub rounding and the branch used for discharge angle. The Cordier end points admit different interpolants, so the coded specific radius should remain identifiable as a design choice. CAD supports the geometry transfer. The archived equivalent-stress legend does not substantiate the claimed elastic margin.

The fourth CFD row preserves the reported 1.76 kW, 3.6057 m and 0.14443 m³/s values, and ranks highest among the printed power values below 4 m. Recombining its printed dimensions gives a shaft torque of about 11.2 N·m at nominal speed and conditional efficiencies of 33.8–34.6%, depending on the hydraulic reference. The sheet's labelled moment would imply 17.6 kW, and its 74.74% efficiency is unresolved. An exported torque and

net-head report on matched control surfaces is necessary before using that row to size a generator or claim an optimum. The 5 kW target is already above the available head power at the original 3.8 m sizing flow for fresh water.

The electrical offtake analysis derives corrected magnetic loading and torque relations. The independently switched R–L test separates carrier and inductance effects and explains the 1 mH versus 10 mH time-constant discrepancy. The measured air coefficient of 0.239 implies about 2.53 W at the reported 10 m/s point. The change in Reynolds and tip-speed ratios limits transfer to water, and the archive's separate 0.56 efficiency figure lacks a reconciled normalisation. Neither the aerodynamic point nor the CFD spreadsheet establishes a qualified MW-scale product.

The fleet calculation of 167 units follows from the assumed rating and equivalent hours. The initial industrial margin calculation is sensitive to unit cost, and a production queue forms if the two teams are modelled as pooled serial resources. These results support a concrete reconciliation sequence. Retrieve the original CFD balance and raw tunnel logs, verify the load case and head reference, align the generator torque-speed point, then use site-specific hydraulic and industrial data for scaling. The original figures, mathematics and listings accompany this calculation record.

References

[1] D. Kumar, T. Ho, S. Daab and W. Abboura. *Integrated Design of a Compact Axial Hydraulic Turbine*. École Nationale Supérieure d’Arts et Métiers, semester 7 project, 2024. Author report, 57 pp. The archived research edition is the source for the figures, displayed equations and listings.

[2] S. L. Dixon and C. A. Hall. *Fluid Mechanics and Thermodynamics of Turbomachinery*. 7th ed., Butterworth-Heinemann, 2014. ISBN 978-0-12-415954-9.

[3] I. B. Celik, U. Ghia, P. J. Roache, C. J. Freitas, H. Coleman and P. E. Raad. Procedure for estimation and reporting of uncertainty due to discretization in CFD applications. *Journal of Fluids Engineering*, 130(7), 078001, 2008. 10.1115/1.2960953.

[4] J. L. Kirtley Jr. *Permanent Magnet “Brushless DC” Motors*. MIT OpenCourseWare, 6.061 Introduction to Electric Power Systems, chapter 12. Course notes.

[5] D. G. Holmes and T. A. Lipo. *Pulse Width Modulation for Power Converters. Principles and Practice*. Wiley-IEEE Press, 2003. IEEE Xplore.

[6] International Electrotechnical Commission. *Hydraulic turbines, storage pumps and pump-turbines – Model acceptance tests*. IEC 60193:2019. IEC catalogue.

Appendix A. Original figure concordance

The original figure numbers in [1] are mapped to the technical panels embedded in this manuscript. Figures with multiple subpanels are indexed individually. The three source p. 26 screen captures have been cropped to their simulation windows.

Table A.1 – Concordance for the archived artwork. Source page numbers count the cover.

Source ID	Source p.	Subject	Open panel
Cover	1	Original turbine and conversion-chain schematic	Figure 1.1
Project overview	3	Original overview render of the ducted runner	Figure 1.2
Fig. 2.1	9	Digitised Cordier diagram	Figure 2.1
Fig. 2.2	10	MATLAB Cordier interpolation	Figure 2.2
Fig. 2.3	11	Graphical head solution	Figure 2.4
Fig. 2.4	11	Table of blade speed and whirl components	Figure 2.5
Fig. 2.5	12	MATLAB angle and axial-speed display	Figure 2.6
Fig. 2.6	12	Blade-section mean-line diagram	Figure 2.8
Fig. 2.7	13	Radial thickness law	Figure 2.9
Fig. 2.8	13	Initial and thicker NACA sections	Figure 2.10
Fig. 2.9	13	Thickness-fit reconstruction	Figure 2.11
Fig. 2.10	14	Fitted coefficient vector	Figure 2.12
Fig. 2.11	14	Replicated runner blade row	Figure 2.14
Fig. 3.1a	15	MATLAB point curves	Figure 3.1a
Fig. 3.1b	15	Imported CATIA surface	Figure 3.1b
Fig. 3.2	16	Finite-element equivalent-stress field	Figure 3.6
Fig. 3.3a	16	Circular pattern in CATIA	Figure 3.2a
Fig. 3.3b	16	Runner and hub	Figure 3.2b
Fig. 3.4	16	Ducted assembly	Figure 3.3
Fig. 3.5	17	Dimensioned drawing	Figure 3.4
Fig. 3.6	17	Fluid-domain solids	Figure 3.5
Fig. 4.1a	18	Computational domain and interfaces	Figure 4.1a
Fig. 4.1b	18	Surface and volume mesh	Figure 4.1b
Fig. 4.2	19	Mesh detail	Figure 4.2
Fig. 4.3a	19	Residuals, monitor and annotated flow case	Figure 4.3a
Fig. 4.3b	19	Sectioned mesh	Figure 4.3b
Fig. 4.4	19	Representative velocity field	Figure 4.4
Fig. 4.5	20	Eight-row CFD spreadsheet	Figure 4.5
Fig. 5.1	21	Permanent-magnet machine section	Figure 5.1
Fig. 5.2	21	Winding layout	Figure 5.2
Fig. 5.3	22	Stator angular convention	Figure 5.3
Fig. 5.4	22	Flux-cutting diagram	Figure 5.4
Fig. 5.5	24	Rectangular air-gap flux-density waveform	Figure 5.5
Fig. 5.6	26	Magnetic finite-element field	Figure 5.7

Table A.2 – Concordance for the archived artwork. Source page numbers count the cover.

Source ID	Source p.	Subject	Open panel
Fig. 5.7a	26	Phase linkage and flux-density field	Figure 5.8a
Fig. 5.7b	26	Electromagnetic torque trace	Figure 5.8b
Fig. 5.8	27	Global speed-control architecture	Figure 5.9
Fig. 5.9	28	Ideal and PWM voltage waveforms	Figure 5.10
Fig. 5.10	28	Voltage traces and spectra	Figure 5.11
Fig. 5.11	28	Ideal and switched phase voltages	Figure 5.12
Fig. 5.12	29	Voltage discrete Fourier transform	Figure 5.13
Fig. 5.13	29	Ideal and PWM phase currents	Figure 5.14
Fig. 5.14a	30	Current with changed carrier and inductance	Figure 5.15a
Fig. 5.14b	30	Voltage in the same comparison	Figure 5.15b
Fig. 5.15	30	Frequency-change comparison	Figure 5.16
Fig. 5.16	31	Converter response at modified voltage limit	Figure 5.17
Fig. 5.17a	31	Torque-study time-trace panel	Figure 5.20a
Fig. 5.17b	31	Torque at zero current-to-EMF angle	Figure 5.20b
Fig. 5.17c	31	Torque comparison at 45° and 90°	Figure 5.20c
Fig. 5.18a	31	Modulation and reference frames	Figure 5.21a
Fig. 5.18b	31	Speed and torque in the regulation sequence	Figure 5.21b
Fig. 5.19	32	Numerical statistics for regulation signals	Figure 5.22
Fig. 5.20	32	Current-reference tracking	Figure 5.23
Fig. 6.1a	33	Runner on the printer build plate	Figure 6.1a
Fig. 6.1b	33	Runner during printing	Figure 6.1b
Fig. 6.1c	33	Printer display	Figure 6.1c
Fig. 6.2	33	Slicing and supports	Figure 6.2
Fig. 6.3a	34	Slicer print-time and material breakdown	Figure 6.3a
Fig. 6.3b	34	Side photograph of the printed rotor	Figure 6.3b
Fig. 6.3c	34	Finished polymer runner	Figure 6.3c
Fig. 6.4	34	CAD view of the tunnel configuration	Figure 6.4
Fig. 6.5	36	Recirculating wind tunnel schematic	Figure 6.5
Fig. 6.6a	36	Prototype and instruments	Figure 6.6a
Fig. 6.6b	36	Alternate view of the instrumentation	Figure 6.6b
Fig. 7.1	38	Original regional comparison	Figure 7.1
Fig. 7.2	40	Comparison of turbine types	Figure 7.2
Fig. 7.3	40	Large and modular turbine comparison	Figure 7.3
Fig. 7.4	41	Compact bulb-turbine concept	Figure 7.4
Fig. 7.5	41	Original sales and stock planning	Figure 7.5

Appendix B. Original equations and tables

These native excerpts preserve the mathematical typography and numeric entries of [1]. The main sections state the quantities used in the recomputations and explain the discrepancies. Source p. 20 is reproduced as Figure 4.5 and fully transcribed in Table 4.1.

Source p. 9 · Rotational speed, similarity and Cordier equation

$$\omega = \frac{2 \times \pi \times \mathrm{N}}{60} = 157.07 \text{ rad.s}^{-1}.$$

$$\Omega = \frac{\omega\sqrt{q_v}}{(gH)^{\frac{3}{4}}} = \frac{\frac{\pi.N}{30}\times\sqrt{q_v}}{(gH)^{\frac{3}{4}}} = \frac{\Phi^{\frac{1}{2}}}{\Psi^{\frac{3}{4}}},$$

$$\mathrm{Nsq} = \frac{N\sqrt{q_v}}{H^{\frac{3}{4}}},$$

which gives

$$\Omega = \frac{\pi.\mathrm{Nsq}}{30.\mathrm{g}^{\frac{3}{4}}} = 3.778.$$

The linear fit used in the selected interval is $\Omega(R_s) = \frac{9.224-1.987}{0.2804-1.31} R_s + 8.705 = -7.03 R_s + 8.70$. Solving $\Omega(R_s) = 3.778$ gives

Source p. 10 · Head, flow and radius relations

$$\mathrm{R_s} = 0.701.$$

$$\Omega = \frac{\omega\sqrt{q_v}}{(gH)^{\frac{3}{4}}}, \qquad \Lambda = \frac{R(gH)^{\frac{1}{4}}}{\sqrt{q_v}}.$$

$$\mathrm{H} = 3.8 \text{ m}$$

$$\mathrm{Nsq} = \frac{N\sqrt{q_v}}{H^{\frac{3}{4}}},$$

$$\mathrm{q_v} = 0.132 \text{ m}^3.\text{s}^{-1}.$$

The hub radius is defined from the hub-to-tip ratio $T = 0.38$: $R_i = R_e T$, with $R_e = 0.1030$ m, hence

$$\mathrm{R_i} = 0.03914 \text{ m}.$$

Source p. 11 · Axial velocity and printed mean-line relation

$$C_a = \frac{q_v}{S} = \frac{q_v}{\pi(R_e^2 - R_i^2)},$$

$$\mathrm{C_a} = 4.629 \text{ m.s}^{-1}.$$

$$d_{yy} = (\tan\beta_2 - \tan\beta_1)\, x_{x2} + \tan\beta_1.$$

Source p. 19 · Mechanical power

$$P_m = C\Omega = M\Omega.$$

Source p. 22 · Magnetic constitutive laws and mechanical EMF

For a linear medium,
$\vec{B} = \mu\vec{H}$.
For air,
$\overrightarrow{B_0} = \mu_0\overrightarrow{H_0}$,
and for the iron,
$\vec{B} = \mu_0\mu_r\vec{H}$, with $\mu_r > 1000$.
For the permanent magnet,

$$\vec{\mathrm{B}} = \mu_0\vec{\mathrm{H}} + \overrightarrow{\mathrm{B_r}}.$$

$$\mathrm{B}(\theta, \mathrm{t}) = \sum_{\mathrm{k}=0}^{\infty} \mathrm{B_{2k+1}} \cos\left[p\,(2\mathrm{k}+1)\,(\theta - \Omega\mathrm{t})\right],$$

$$\mathrm{e} = \mathrm{l}\left|\vec{\mathrm{B}} \Lambda \vec{\mathrm{v}}\right| = \mathrm{lBv} \text{ if } \vec{\mathrm{B}} \perp \vec{\mathrm{v}}.$$

With $LxB = \phi$,
$\frac{d\phi}{dt} = \frac{dx}{dt} LB = vLB.$

Source p. 23 · Phase EMFs, balanced currents and mean torque

$$\mathrm{e_{condA}} = \mathrm{B}(0,\mathrm{t}) * \frac{\Omega \mathrm{D}}{2}\mathrm{L}, \qquad \mathrm{e_{phaseB}} = \mathrm{nB}\left(\frac{2\pi}{3\mathrm{p}},\mathrm{t}\right)\frac{\Omega \mathrm{D}}{2}\mathrm{L},$$

$$e_{condA'} = B\left(\frac{\pi}{2},t\right)\frac{\Omega D}{2}L = -e_{condA}. \qquad \mathrm{e_{phaseC}} = \mathrm{nB}\left(\frac{4\pi}{3\mathrm{p}},\mathrm{t}\right)\frac{\Omega \mathrm{D}}{2}\mathrm{L}.$$

$$\mathrm{e_{phaseA}} = \Sigma \mathrm{e_{condA}} - \Sigma \mathrm{e_{condA'}} = \mathrm{nB}(0,\mathrm{t})\frac{\Omega \mathrm{D}}{2}\mathrm{L}. \qquad i_i(t) = I\sqrt{2}\cos\left(\omega t - \Psi - (i-1)\frac{2\pi}{3}\right), \qquad \omega = p\Omega.$$

$$P_{em}(t) = \sum_{i=1}^{3} e_i i_i = n\frac{\Omega D}{2}L\sum_{i=1}^{3}\sum_{k=0}^{\infty} B_{k+1}\cos\left[(2k+1)\left((i-1)\frac{2\pi}{3} - \omega t\right)\right]\cos\left(\omega t - \Psi - (i-1)\frac{2\pi}{3}\right).$$

$$\langle p_{em}\rangle = I\sqrt{2}n\frac{\Omega D}{2}L\sum_{i=1}^{3} B_1\cos\left((i-1)\frac{2\pi}{3} - \omega t\right)\cos\left(\omega t - \Psi - (i-1)\frac{2\pi}{3}\right),$$

$$\langle \mathrm{p_{em}}\rangle = \frac{3}{2}\mathrm{I}\sqrt{2}\mathrm{n}\frac{\Omega \mathrm{D}}{2}\mathrm{L}\cos(\Psi). \qquad \langle C_{em}\rangle = \frac{\langle p_{em}\rangle}{\Omega} = \frac{3}{2\sqrt{2}}nB_1IDL\cos\Psi = \frac{3}{2\sqrt{2}}\frac{A\pi D}{3}DB_1L\cos\Psi,$$

Using the linear current loading $A = \frac{3nI}{\pi D}$ and bore volume $V = \frac{\pi D^2 L}{4} = \pi R^2 L$,

$$\langle \mathrm{C_{em}}\rangle = \sqrt{2}\mathrm{B_1AV}\cos(\Psi).$$

$$\langle \mathrm{C_{em}}\rangle_{\max} = \sqrt{2}\mathrm{B_1AV}.$$

Source p. 24 · Gap field and Fourier coefficient

$$\overrightarrow{rot}\left(\overrightarrow{H}\right) = \overrightarrow{J} \rightarrow \begin{cases} \overrightarrow{B} = \mu_0\overrightarrow{H} \text{ in air} \\ \overrightarrow{B} = \mu_0\mu_r\overrightarrow{H} \text{ in iron, } \mu_r > 1000 \\ \overrightarrow{B} = \mu_0\overrightarrow{H} + \overrightarrow{B_r} \text{ in the magnet} \end{cases} \qquad \oint \overrightarrow{H}\cdot\overrightarrow{dl} = 0.$$

The field intensity in the iron is negligible compared with that in the air gap:
$H_{fer} = \frac{B_{fer}}{\mu_0\mu_r} \ll H_{air}$.
The magnetic-circuit equation therefore reduces to

$$2\mathrm{H_a e_a} + 2\mathrm{H_g g} = 0, \qquad \mathrm{B_a} = \mathrm{B_g} = \widehat{\mathrm{B}}.$$

$$a_1 = \frac{2}{T}\int_{-T/2}^{T/2} f(T)\cos(\omega t)dt,$$

$$\begin{cases} B_g = \mu_0 H_g \rightarrow H_g = \frac{\widehat{B}}{\mu_0} \\ B_a = \mu_0 H_a + B_r \\ H_a = \frac{\widehat{B} - B_r}{\mu_0} \end{cases}, \qquad B_1 = a_1 = \frac{2}{\frac{2\pi}{p}}\int_{-\frac{\pi}{p}}^{\frac{\pi}{p}} B(\theta)\cos(p\theta)d\theta = \frac{4}{\pi}\widehat{B}\sin\left(\frac{\beta\pi}{2}\right),$$

$$\widehat{\mathrm{B}} = \frac{\mathrm{e_a B_r}}{\mathrm{g} + \mathrm{e_a}}. \qquad \mathrm{B_1} = \frac{4}{\pi}\widehat{\mathrm{B}}\sin\left(\frac{\beta\pi}{2}\right).$$

Source p. 25 · Stator fill, losses and torque-speed sizing

Symbol	Definition
J	RMS current density in the conductors (A/mm²)
A_L	linear current loading
k_r	slot fill factor
D	air-gap diameter
$B_{e,max}$	maximum air-gap induction
B_r	magnet remanent flux density
g	air-gap length
B_{sat}	saturation flux density
f_{max}	maximum electrical frequency

$$\Delta T \sim \frac{P_J}{hS_{ext}}, \qquad S_{ext} \sim \pi DL,$$

$$\Delta \mathrm{T} \sim \frac{\rho \mathrm{AJ}}{\mathrm{h}}.$$

$$J \in [3\times10^6, 7\times10^6]\ \mathrm{A/m^2},$$

$$A \in [12{,}000, 60{,}000]\ \mathrm{A/m}.$$

$$P_N = C_{em}\Omega_N, \qquad C_{em} = \frac{P_N}{\Omega_N} = \frac{P_N}{\frac{\pi N}{30p}},$$

$$k_r = \frac{\sum S_{cond}}{S_{slots}},$$

$$\mathrm{C_{em}} = 152\ \mathrm{Nm}.$$

$$P_J = 3nR_{cond}I^2 = 3n\rho\frac{L}{S_{cond}}I^2 = \rho 3nILJ = \rho\pi DL\,AJ,$$

$$X = \frac{\widehat{B}}{B_r},$$

Source p. 26 · Printed torque and active length

$$\widehat{B} = XB_r, \qquad B_1 = \frac{4}{\pi}\widehat{B}\sin\left(\frac{\beta\pi}{2}\right),$$

$$\mathrm{L} = \frac{\mathrm{C}}{\sqrt{2}\mathrm{AXB_rD^2}\sin\left(\frac{\beta\pi}{2}\right)}.$$

$$C_{em} = \sqrt{2}AD^2LB_r\sin\left(\frac{\beta\pi}{2}\right),$$

The rotating-system dynamics may be expressed in the generic form
$J\frac{d\Omega}{dt} = C_{em} - C_{load}$,
where J is the total rotating inertia, Ω the rotational speed, C_{em} the electromagnetic torque, and C_{load} the

Source p. 27 · Phase linkage, back-EMF and electric power

$$\varphi_i = \varphi_m\sqrt{2}\cos\left(\theta - (i-1)\frac{2\pi}{3}\right),$$

$$e_i = -\frac{d\varphi_i}{dt} = \frac{d\varphi_i}{d\theta}\frac{d\theta}{dt} = \sqrt{2}\varphi_m\omega\sin\left(\theta - (i-1)\frac{2\pi}{3}\right).$$

The electrical power relations are
$P = 3VI\cos\alpha$,

$$P_e = 3EI\cos\psi,$$

$$\mathrm{C_{em}} = \frac{\mathrm{P_e}}{\Omega} = 3\frac{\mathrm{E}}{\Omega}\mathrm{I}\cos\psi.$$

Source p. 29 · Printed phase-circuit values

$$f_c = \frac{R}{2\pi L} = \frac{10}{2\pi\cdot 0.001} = 150\,\mathrm{Hz},$$

$$\tau = \frac{L}{R} = \frac{0.001}{10} = 1\,\mathrm{ms}.$$

Source p. 34 · Experimental coefficient nomenclature

Quantity	Definition	Expression or source
C_p	power coefficient	$P/(0.5\rho S V^3)$
P	mechanical power recovered at the shaft	$C\omega$
C	rotor torque	experiment
ω	rotational speed	$\pi N/30$
V	upstream reference velocity	experiment

Source p. 35 · Power coefficient, Pitot relation and available energy

Quantity	Definition	Expression or source
U	blade-tip circumferential speed	$R\omega$
λ	tip-speed ratio	U/V
S	rotor-disc area	$\pi(2R)^2/4$
R	blade-tip radius	75 mm
ρ	air density	1.2 kg/m^3
C_c	torque coefficient	derived from C_p

$C_{p,max} = 0.239.$

$$P_{available} = \frac{1}{2}\rho_{air} S V_{wind}^3.$$

$$V_{wind} = \sqrt{\frac{2\Delta P}{\rho_{air}}}.$$

Source p. 38 · Reference product assumptions, first row

Characteristic	Assumed value
nominal head	1.5-10 m

Source p. 39 · Reference fleet and deployment schedule

Characteristic	Assumed value
unit power	2 MW
maximum efficiency	85-90%
estimated cost per turbine	EUR 2 million
design life	30-40 years

2 MW × 6000 h = 12 GWh/year.

$$\text{Number of turbines} = \frac{2000}{12} \approx 167.$$

Year	Turbines produced	Cumulative installed turbines	Cumulative annual production (GWh)
2025	33	33	396
2026	33	66	792
2027	33	99	1,188
2028	34	133	1,596
2029	34	167	2,004

Source p. 41 · Production cadence, steel and labour totals

Year	Annual quantity	Quarterly quantity	Average monthly quantity
2025	33	8-9	2.75
2026	33	8-9	2.75
2027	33	8-9	2.75
2028	34	8-9	2.83
2029	34	8-9	2.83

$20\ \text{t/turbine} \times 167 = 3340\ \text{t}.$

Operation	Required operators	Hours per turbine
component machining	20	50
assembly	30	40
painting and surface treatment	10	20
quality control	10	10
Total stated in the original schedule	**85**	**120**

Source p. 42 · Operation hours, takt and lead time

- machining: $50 \times 3 = 150$ h/month;
- assembly: $40 \times 3 = 120$ h/month;
- painting and treatment: $20 \times 3 = 60$ h/month;
- quality control: $10 \times 3 = 30$ h/month.

$$35\ \text{h/week} \times 4 = 140\ \text{h/month}.$$

$$35\ \text{h/week} \times 4\ \text{weeks/month} \times 2 = 280\ \text{h/month}.$$

$$\text{Takt time} = \frac{280}{3} = 93.33\ \text{h/turbine}.$$

$$50 + 40 + 20 + 10 = 120\ \text{h/turbine}.$$

Source p. 43 · Cost allocation and sourcing

Cost item	Cost per turbine	Share
machining	EUR 0.8 million	40%
assembly	EUR 0.6 million	30%
electrical systems	EUR 0.4 million	20%
surface treatment and quality	EUR 0.2 million	10%
Total	**EUR 2.0 million**	**100%**

$$167 \times \text{EUR 2 million} = \text{EUR 334 million}.$$

Component	Make	Buy	Rationale
turbine runner	internal machining	-	direct control of quality and geometry, at higher capital cost
fixed and moving blades	internal production	-	dimensional flexibility and performance control
casing	-	local supplier	lower cost, with supplier dependency
electrical generator	-	qualified supplier	access to specialist capability, with lead-time risk
control systems	-	specialist partners	expertise and certification requirements
lubrication system	internal integration	-	environmental and system-level control

Source p. 44 · Location table and commercial balances

Country	Advantages	Disadvantages
France	proximity to installation sites; strong industrial expertise and quality control	high labour cost
Poland	competitive labour cost; developed industrial infrastructure	moderately more complex logistics
Turkey	highly competitive metal-processing cost; good access to steel	greater transport distance
China	very low cost for standard components; extensive industrial capacity	long lead times, quality risk, and trade exposure
Portugal	balanced labour cost and European proximity	somewhat lower heavy-industrial capacity

- selling price: EUR 3 million per turbine;
- total sales: 167 turbines;
- total revenue: $167 \times 3 =$ EUR 501 million;
- manufacturing cost: EUR 2 million per turbine;
- total manufacturing cost: $167 \times 2 =$ EUR 334 million;
- R&D and initial investment: EUR 30 million;
- fixed costs over five years: EUR 50 million.

$$\text{EUR 3 million} - \text{EUR 2 million} = \text{EUR 1 million}.$$

$$167 \times \text{EUR 1 million} = \text{EUR 167 million}.$$

$$\text{EUR 501 million} - (\text{EUR 334 million} + \text{EUR 30 million} + \text{EUR 50 million}) = \text{EUR 87 million}.$$

$$ROI = \frac{\text{Net profit}}{\text{Total investment}} \times 100,$$

$$ROI = \frac{87}{334 + 30 + 50} \times 100 \approx 21.5\%.$$

$$33 \text{ turbines/year} \times \text{EUR 1 million/turbine} = \text{EUR 33 million/year},$$

Source p. 45 · Payback and summary

$$\text{Payback} = \frac{30 + 50}{33} \approx 2.4 \text{ years}.$$

Indicator	Value
total revenue	EUR 501 million
total cost	EUR 414 million
total net profit	EUR 87 million
ROI	21.5%
payback period	2.4 years

Appendix C. Original MATLAB and XFoil listings

Listings A.1–A.4 from [1] retain their own line numbers and captions. They cover preliminary sizing and CATIA export, profile fitting, mean-line generation and thickness offset. The XFoil point file and the separate plotting/import helpers were referenced in the original code and were unavailable in the archive.

```
clear all; close all; clc

%%%%%%%%%%%%%%%%%%%%%%%%%%%%%%%%%%%%%%%%%%%%%%%%%%%%%%%%%%%%%%%%%%%%%%%%%%%%

%Preliminary sizing of an axial turbine

%   - Complete the following script and the functions it calls

%   - Execute line by line using the F9 key

%%%%%%%%%%%%%%%%%%%%%%%%%%%%%%%%%%%%%%%%%%%%%%%%%%%%%%%%%%%%%%%%%%%%%%%%%%%%

% options

Nom='marim';%Turbine name

%constants

g=9.81; %m^2/s

%%%%%%%%%%%%%%%%%%%%%%%%%%%%%%%%%%%%%%%%%%%%%%%%%%%%%%%%%%%%%%%%%%%%%%%%%%%%

%Design specification

%%%%%%%%%%%%%%%%%%%%%%%%%%%%%%%%%%%%%%%%%%%%%%%%%%%%%%%%%%%%%%%%%%%%%%%%%%%%

N=1500;%rpm

%Q1: Determine the angular velocity

omega=N*2*pi/60;%rad/s

Re=0.103;% penstock radius and turbine outer radius

Nsq=200;%engineering specific speed

%Q2: Determine the angular velocity

vas=Nsq*2*pi/60/g^.75;%specific angular velocity

disp(vas);

vas = Nsq*2*pi/60/g^.75; % specific speed

%% Sizing using the Cordier diagram

% q1 determine the specific radius from the Cordier diagram

Lambda = 0.701;

% q2 - Determine the head parameters (H and qv) as functions of
% vas, Lambda, and R
```

```
%%%%%%%%%%%%%%%%%%%%

% graphical solution for H

H = 0.1:0.1:10; % definition of a variable

A = vas/omega*(g*H).^.75 - Re/Lambda*(g*H).^0.25; % exploitation
% of the two-equation system

figure(2);

plot(H, A, 'b');

line([0 10], [0 0]);

xlabel('H (m)');

ylabel('A');

clear H;

%therefore

H=3.8;% design head

% deduce qv

qv=(Nsq*H^0.75/N)^2;

disp(qv);

%%%%%%%%%%%%%%%%%%%%%%%%%%%%%%%%%%%%%%%%%%%%%%%%%%%%%%%%%%%%%%%%%%%%%%%%%%%%

%% Global preliminary sizing of the runner

Za = 6; % number of blades

eta = 0.92; % hydraulic efficiency

% aspect ratio T = Ri/Re:

T = 0.38;

Ri = Re*T;

Ri = floor(1000*Ri)/1000; % rounded to the nearest millimetre

disp('Re (m), Ri (m)');

disp([Re Ri]);

% q5: Create a series of five radii from Ri to Re to discretise

% the blade angle (rounded to the nearest millimetre)

nr = 5; % number of radial discretisation points

r = linspace(Ri, Re, nr);

r = floor(r*1000)/1000;

%%%%%%%%%%%%%%%%%%%%%%%%%%%%%%%%%%%%%%%%%%%%%%%%%%%%%%%%%%%%%%%%%%%%%%%%%%%%

% Blade velocity triangles and runner-blade plotting

```

```
%%%%%%%%%%%%%%%%%%%%%%%%%%%%%%%%%%%%%%%%%%%%%%%%%%%%%%%%%%%%%%%%%%%%%%%%%%%%%%%

%Q6: Calculate the axial flow component of fluid velocity (Ca) from

% qv, Re, and Ri

Ca = qv / (pi * (Re^2 - Ri^2));

disp(Ca);

%%%%%%%%%%%%%%%%%%%%%%%%%%%%%%%%%%%%%%%%%%%%%%%%%%%%%%%%%%%%%%%%%%%%%%%%%%%%%%%

%Definition of blade sections at radius r(u)

%%%%%%%%%%%%%%%%%%%%%%%%%%%%%%%%%%%%%%%%%%%%%%%%%%%%%%%%%%%%%%%%%%%%%%%%%%%%%%%

% Complete the loop that defines the nr sections line by line

%sections

% NOTE: during the first pass, disable "for" and "end" for debugging

% for-loop generating the nr intermediate blade profiles

% for-loop generating the nr intermediate blade profiles

for u = 1:size(r, 2)

    %u=1

    % Q7: At the current radius r, calculate the kinematic components U(r),
    % and Cu2_th(r)

    % then Cu2(r), accounting for hydraulic efficiency eta (recall that
    %

    % the machine is purely axial: Ca(r)=Ca1(r)=Ca2(r) and U(r)=
    % U1(r)=U2(r)

    U = omega*r(u);

    Cu2_th = -g*H/U; % (Euler theorem)

    Cu2 = Cu2_th*eta;

    % Q8: Determine the blade inlet angle beta_1 and outlet angle
    % beta_2

    beta_1 = atand(U/Ca);

    beta_2 = atand((U - Cu2)./Ca);

    % the discharge angle alpha_2,

    alph_2 = atand(Ca/Cu2);

    % Display values in the Command Window for verification.
    % Accept beta_1 and beta_2 within the range [30 deg, 80 deg].

    if u==1; disp('check: r(u)   beta_1    beta_2    alph_2');end;

    disp([r(u) beta_1 beta_2 alph_2]);

    %%%%%%%%%%%%%%%%%%%%%%%%%%%%%%%%%%%%%%%%%%%%%%%%%%%%%%%%%%%%%%%%%%%%%%%%%%%%%%%

    %Mean-line processing
```

```
%%%%%%%%%%%%%%%%%%%%%%%%%%%%%%%%%%%%%%%%%%%%%%%%%%%%%%%%%%%%%%%%%%%%%%%%%%%%%%%%

%Discretisation of the unit axial-extent mean line xx

%Refine near the leading edge

%arbitrary discretisation that may be modified

xba=[0,logspace(-6,-2,10)];% leading-edge region

xmc=linspace(0.011,0.1,9);% mid-chord region

xbf=linspace(0.11,1,9);% trailing-edge region

xx=[xba xmc xbf];

% Calculate the mean line using the ligneK function

%%%%%%%%%%%%%%%%%%%%%%%%%%%%%%%%%%%%%%%%%%%%%%%%%%%%%%%%%%%%%%%%%%%%%%%%%%%%%%%%

%Q9: Edit and complete the LigneK script before executing the

%following command

[yy,beta_i]=ligneK(beta_1,beta_2,xx);

%Plot the unit axial-extent mean line

figure (2); hold on;

plot(xx,yy,'r');xlabel('xx[ ]');ylabel('yy[ ]');

legend('unit axial-extent mean line');

axis equal

%%%%%%%%%%%%%%%%%%%%%%%%%%%%%%%%%%%%%%%%%%%%%%%%%%%%%%%%%%%%%%%%%%%%%%%%%%%%%%%%

%Thickness distribution along the mean line

%%%%%%%%%%%%%%%%%%%%%%%%%%%%%%%%%%%%%%%%%%%%%%%%%%%%%%%%%%%%%%%%%%%%%%%%%%%%%%%%

%Q10: Set the radial variation of relative thickness tt(r) from the root

%of the blade (arbitrarily 13%) to the tip (arbitrarily 3%).

%

%This distribution may be improved at the end of the practical session

ep_pied=13/100;

ep_peri=3/100;

tt=linspace(ep_pied,ep_peri,nr);

figure (3);hold on;

legend('thickness law')

plot(r,tt);

xlabel('r(m)');ylabel('ep(%)');

%tt=[0.16 0.11 0.08 0.05 0.03];% an alternative tt(r) variation

%Q11: Answer Questions Q11.1 and Q11.2. Edit the epaisseurK function
```

```
    %and complete its script to answer Question Q11.3
    [xp1 yp1 xp2 yp2]=epaisseurK(xx,yy,beta_i,tt(u));
    %transpose into column vectors
    xp1=xp1'; yp1=yp1';
    xp2=xp2'; yp2=yp2';
    figure (4); hold on;
    plot(xp1,yp1,'b')
    plot(xp2,yp2,'g')
    axis equal
%%%%%%%%%%%%%%%%%%%%%%%%%%%%%%%%%%%%%%%%%%%%%%%%%%%%%%%%%%%%%%%%%%%%%%%%%%%%
    %Blade-row solidity
%%%%%%%%%%%%%%%%%%%%%%%%%%%%%%%%%%%%%%%%%%%%%%%%%%%%%%%%%%%%%%%%%%%%%%%%%%%%
    %Q12: Recall the definition and role of solidity, including its benefits and drawbacks.
    %drawbacks of high solidity.
    serrage=0.6;
    lx=serrage*(2*pi*r(u)/6);%chord length
    xp1=xp1*lx; yp1=yp1*lx;%scale the profiles
    xp2=xp2*lx; yp2=yp2*lx;
    zz=ones(size(xx')).*r(u);%for 3D plotting
    %for visualisation
    figure (5); hold on;
    plot3(xp1,yp1,zz,'r')
    plot3(xp2,yp2,zz,'k')
    %Additionally, plot the Ri and Re envelope circles
    %angular discretisation
    theta=0:0.01:2*pi;
    yri=Ri*cos(theta);
    zri=Ri*sin(theta);
    xri=zeros(1,size(theta,2));
    plot3(xri,yri,zri);
    plot3(xri,yri/Ri*Re,zri/Ri*Re);
    axis equal
    view(120,16)
```

```
317
318 %%%%%%%%%%%%%%%%%%%%%%%%%%%%%%%%%%%%%%%%%%%%%%%%%%%%%%%%%%%%%%%%%%%%%%%%%%%%
319
320     %projection of the profile onto the hub
321
322 %%%%%%%%%%%%%%%%%%%%%%%%%%%%%%%%%%%%%%%%%%%%%%%%%%%%%%%%%%%%%%%%%%%%%%%%%%%%
323
324     %projection angles
325
326     the21=yp1./unique(zz);
327
328     the22=yp2./unique(zz);
329
330     %initialise a zero matrix for each envelope
331
332     XXext=zeros(size(xx,2),3); XXint=zeros(size(xx,2),3);
333
334     %cylindrical projection
335
336     XXext(:,1)=xp1;
337
338     XXint(:,1)=xp2;
339
340     XXext(:,2)=r(u)*cos(the21);
341
342     XXint(:,2)=r(u)*cos(the22);
343
344     XXext(:,3)=r(u)*sin(the21);
345
346     XXint(:,3)=r(u)*sin(the22);
347
348     % final plot
349
350     figure (6); hold on;
351
352     plot3(xri,yri,zri);
353
354     plot3(xri,yri/Ri*Re,zri/Ri*Re);
355
356     plot3(XXext(:,1),XXext(:,2),XXext(:,3),'b')
357
358     plot3(XXint(:,1),XXint(:,2),XXint(:,3),'g')
359
360     axis equal
361
362     view(-30,0)% viewpoint
363
364     %Blade replication
365
366     traceZpales(XXext,Za,[0 0 0]);
367
368     traceZpales(XXint,Za,[1 0 0]);
369
370     view(100,60)
371
372 %%%%%%%%%%%%%%%%%%%%%%%%%%%%%%%%%%%%%%%%%%%%%%%%%%%%%%%%%%%%%%%%%%%%%%%%%%%%
373
374     %create a structure for storing the CATIA point clouds
375
376     XXX.ext(u).R=XXext*1000;
377
378     XXX.int(u).R=XXint*1000;
379
380 end
381
382 %%%%%%%%%%%%%%%%%%%%%%%%%%%%%%%%%%%%%%%%%%%%%%%%%%%%%%%%%%%%%%%%%%%%%%%%%%%%
```

```
383
384     %Generate an export file for CATIA
385
386 Nom='Courbes-GSD';%Excel file name
387
388 TableauGSD={'StartLoft','',''};
389
390 for u=1:nr
391
392     %upper surface
393
394     TableauGSD=[TableauGSD ; {'StartCurve','',''}];
395
396     for k=1:length(XXX.ext(u).R)
397
398         TableauGSD=[TableauGSD ;
399 {XXX.ext(u).R(k,1),XXX.ext(u).R(k,2),XXX.ext(u).R(k,3)}];
400
401     end
402
403     TableauGSD=[TableauGSD ; {'EndCurve','',''}];
404
405     %lower surface
406
407     TableauGSD=[TableauGSD ; {'StartCurve','',''}];
408
409     for k=1:length(XXX.int(u).R)
410
411         TableauGSD=[TableauGSD ;
412 {XXX.int(u).R(k,1),XXX.int(u).R(k,2),XXX.int(u).R(k,3)}];
413
414     end
415
416     TableauGSD=[TableauGSD ; {'EndCurve','',''}];
417
418 end
419
420 TableauGSD=[TableauGSD ; {'EndLoft','',''}];
421
422 TableauGSD=[TableauGSD ; {'End','',''}];
423
424 xlswrite(Nom,TableauGSD); % copy these data into the CATIA file
425 % GSD_PointSplineLoftFromExcel.xls, which contains the import macro.
```

Listing A.1: Axial-turbine preliminary sizing and CATIA point-cloud export routine.

```
1  %Find an analytical expression for profiles whose
2
3  %trailing edge is thickened to ensure mechanical strength.
4
5  % Input: point file generated by XFOIL (\"psave\")
6
7  % Tool: MATLAB fminsearch or lsqcurvefit if the Optimization Toolbox is available.
8
9  clear all; close all; clc;
10
11 %Q11.21: enter the filename and corresponding relative thickness
12
13 fname='NACA0015_DEV_KUMAR.txt';
14
15 tt=0.15;%relative thickness of the profile to load
16
17 data=load(fname);%load the file
18
19 figure(1);hold on;%plot raw points
```

```
plot(data(:,1),data(:,2));

axis equal

%Q11.22: Define xdata and ydata for the upper surface (first half of the file points).

xdata=data(1:ceil(239/2),1);

ydata=data(1:ceil(239/2),2);

plot(xdata,ydata,'g-');% plot in red

%Q11.23: Plot the unmodified NACA thickness law; its coefficients initialise the fit.

naca0=[0.2969 -0.1260 -0.35116 +0.2843 -0.1015]; % standard NACA coefficients

% define the fonc_naca function with:

% tt=relative thickness, %

% x=chordwise abscissae

% Variables are defined inside @(), followed by the function expression.

fonc_naca=@(naca,x) tt/0.2*(naca(1)*x.^0.5+naca(2)*x+naca(3)*x.^2+naca(4)*x.^3+naca(5)*x.^4);

y0=fonc_naca(naca0,xdata); % recover the thickness distribution from naca0

plot(xdata,y0,'m-');%plot in green

%Q11.24: Configure fminsearch to obtain the new coefficients.

% The new ecartq function (sum of squared differences between
% data and model) is minimised to define the coefficients of the

% modified profile

ecartq= @(naca) sum((ydata-fonc_naca(naca,xdata)).^2);

naca_mod=fminsearch(ecartq, naca0);%See the fminsearch documentation

disp(naca_mod);%display the coefficients

plot(xdata,fonc_naca(naca_mod,xdata),'r*:') % zoom in to compare data and model
```

Listing A.2: Modified NACA thickness-law identification routine.

```
function [yy,beta_i]=ligneK(beta_1,beta_2,xx)

%plots the mean lines yy=f(xx) of the blade sections:

%with:

    % inputs:

    % beta_1:inlet angle

    % beta_2:outlet angle

    % xx normalised abscissae

    % outputs:

    % yy ordinates
```

```
    % beta_i angles
%boundary conditions:
    % linear variation of local angle beta_i between beta_1 and beta_2
%define:
    % dyy local variation
%%%%%%%%%%%%%%%%%%%%%%%%%%%%%%%%%%%%%%%%%%%%%%%%%%%%%%%%%%%%%%%%%%%%%%%%%%%%%%%
%Q :Define dyy=f(xx), then yy=f(xx)
    dyy=(tand(beta_2)-tand(beta_1)).*xx+tand(beta_1);
    yy=0.5*(tand(beta_2)-tand(beta_1)).*xx.^2+tand(beta_1).*xx;
 %%%%%%%%%%%%%%%%%%%%%%%%%%%%%%%%%%%%%%%%%%%%%%%%%%%%%%%%%%%%%%%%%%%%%%%%%%%%%%%
 %Q :Define the local angle beta_i=f(dyy)
     beta_i=atand(dyy);
end
```

Listing A.3: Blade-section mean-line generator.

```
function [xp1 yp1 xp2 yp2]=epaisseurK(xx,yy,bei,tt)
%distributes the NACA thickness along the mean lines
%with:
    % inputs:
    % xx: normalised mean-line abscissae (0 to 1)
    % yy: mean-line ordinates based on xx
    % beta_i: local angle
    % tt: relative thickness
    % outputs:
    % xp1 and yp1: upper-surface point coordinates
    % xp2 and yp2: lower-surface point coordinates
%Q11.3: Enter the yt polynomial coefficients in the row vector naca.
%See the Loi_Ep2.m script to determine them
%naca=[0.3025   -0.1350   -0.3610   0.2887   -0.0781];
naca=[0.2947   -0.1129   -0.3719    0.3214   -0.0981];
%naca=[0.2969  -0.1260  -0.35116   0.2843  -0.1015];%standard coefficients
yt=tt/0.2*(naca(1)*xx.^0.5+naca(2)*xx+naca(3)*xx.^2+naca(4)*xx.^3+naca(5)*xx.^4);
%%%%%%%%%%%%%%%%%%%%%%%%%%%%%%%%%%%%%%%%%%%%%%%%%%%%%%%%%%%%%%%%%%%%%%%%%%%%%%%
```

```
%%%%%%%%%%%%%%%%%%%%%%%%%%%%%%%%%%%%%%%%%%%%%%%%%%%%%%%%%%%%%%%%%%%%%%%%%%%%%%%%

% Calculate local chord length cc for scaling

    cc=(xx(end)^2+yy(end)^2).^0.5;

% Calculate the coordinates of each envelope point

    %upper surface xp1, yp1

    xp1=xx-cc*yt.*sind(bei);

    yp1=yy+cc*yt.*cosd(bei);

    %lower surface: xp2, yp2

    xp2=xx+cc*yt.*sind(bei);

    yp2=yy-cc*yt.*cosd(bei);

    % normalise by the chord length

    xp1=xp1/cc;

    yp1=yp1/cc;

    xp2=xp2/cc;

    yp2=yp2/cc;

end
```

Listing A.4: Blade-thickness distribution about the mean line.

A.1 Software environment and model scope

The study combines MATLAB for numerical sizing and data processing, XFoil for section-profile manipulation, CATIA V5 for surface and solid modelling, STAR-CCM+ for computational fluid dynamics, SIMBA for the electromechanical drive and PWM investigations, and PrusaSlicer for additive-manufacturing preparation. Each numerical stage is a preliminary engineering model and should be interpreted within the assumptions stated in the corresponding chapter. In particular, the steady moving-reference-frame CFD model, the two-dimensional magnetic approximation, the wind-tunnel similarity experiment, and the high-level industrial business case are complementary design tools rather than substitutes for full-scale qualification.

Appendix D. Reproducibility

The PDF contains **turbine_study.py**, **turbine_results.json** and the 57-page **Compact_Axial_Hydraulic_Turbine_Source.pdf**. The last file is a source copy with the three p. 26 images masked outside the technical windows. The source itself documents the CAD, CFD, converter and wind-tunnel stages.

D.1 Running the Python study

```
python turbine_study.py --output results
```

Extract the script using the attachments pane of a desktop PDF reader. It uses NumPy, SciPy and Matplotlib and requires no external inputs. The JSON file records version information, the transcribed CFD rows, and the calculations behind all thirteen figures.

D.2 Numerical checks

The geometry functions check the spanwise energy relation and the first archived velocity-triangle row. The CFD routine checks the power-to-moment ratio across the whole sheet. The PWM test verifies zero neutral-current sum, fundamental impedance and convergence under time-step refinement. The production model uses a calendar in working hours and verifies the undiscounted commercial balance. Source values and independent model outputs have different captions throughout.